

1 **Enhancements of the refractory submicron aerosol fraction in the Arctic polar**
2 **vortex: feature or exception?**

3 R. Weigel¹, C. M. Volk², K. Kandler³, E. Hösen^{2*}, G. Günther⁴, B. Vogel⁴, J.-U. Groöß⁴, S. Khaykin^{5**},
4 G. V. Belyaev⁶ and S. Borrmann^{1,7}

5 ¹Institut für Physik der Atmosphäre, Johannes Gutenberg-Universität, Mainz, Germany

6 ²Department of Physics, University of Wuppertal, Germany

7 ³Institut für Angewandte Geowissenschaften, Technische Universität Darmstadt, Germany

8 ⁴Institut für Energie- und Klimaforschung (IEK-7), Forschungszentrum Jülich, Germany

9 ⁵Central Aerological Observatory, Dolgoprudny, Moscow Region, Russia

10 ⁶Myasishchev Design Bureau, Zhukovsky-5, Moscow Region, Russia

11 ⁷Partikelchemie, Max-Planck-Institut für Chemie, Mainz, Germany

12 *now at the Institut für Ozeanographie, Universität Hamburg, Germany

13 **now at the CNRS/INSU, LATMOS-IPSL, Université de Versailles St. Quentin, Guyancourt, France

14 **Abstract**

15 In-situ measurements with a 4-channel stratospheric condensation particle counter (CPC) were
16 conducted at up to 20 km altitude on board the aircraft M-55 *Geophysica* from Kiruna, Sweden,
17 in January through March (EUPLEX 2003, RECONCILE 2010) and in December (ESSenCe 2011).
18 During all campaigns air masses from the upper stratosphere and mesosphere were subsiding
19 inside the Arctic winter vortex, thus initializing a transporting of refractory aerosol into the
20 lower stratosphere ($\theta < 500$ K). The strength and extent of this downward transport varied
21 between the years depending on the dynamical evolution of the vortex. Inside the vortex and at
22 potential temperatures $\theta \geq 450$ K around 11 submicron particles per cm^3 were generally
23 detected. Up to 8 of these 11 particles per cm^3 were found to contain thermo-stable (at 250°C)
24 residuals with diameters of 10 nm to about $1 \mu\text{m}$. Particle mixing ratios (150 mg^{-1}) and fractions
25 of non-volatile particles (75 % of totally detected particles) exhibited highest values in air
26 masses having the lowest content of nitrous oxide (70 nmol mol^{-1} of N_2O). This indicates that
27 refractory aerosol originates from the upper stratosphere or the mesosphere. Derived from the
28 mixing ratio of the simultaneously measured long-lived tracer N_2O an empirical index serves to
29 differentiate probed air masses according to their origin: inside the vortex, the vortex edge
30 region, or outside the vortex. Previously observed high fractions of refractory submicron aerosol
31 in the 2003 Arctic vortex were ascribed to unusually strong subsidence during that winter.
32 However, measurements under perturbed vortex conditions in 2010 and during early winter in
33 December 2011 revealed similarly high values. Thus, the abundance of refractory aerosol in the
34 lower stratosphere within the Arctic vortices appears to be a regular feature rather than the
35 exception. During December, the import from aloft into the lower stratosphere appears to be
36 developing; thereafter the abundance of refractory aerosol inside the vortex reaches its highest
37 levels in March. The correlations of refractory aerosol with N_2O suggest that, apart from mean
38 subsidence, diabatic dispersion inside the vortex significantly contributes to the transport of
39 particles to the Arctic lower stratosphere. A measurement-based estimate of the total mass of
40 refractory aerosol inside the vortex is provided for each campaign. Based on the derived
41 increase of particle mass in the lower stratospheric vortex (100 – 67 hPa pressure altitude) by a
42 factor of 4.5 between early and late winter, we estimate the total mass of mesospheric particles
43 deposited in the Arctic vortex. This estimate is compared with the expected atmospheric influx
44 of meteoritic material ($110 \pm 55 \times 10^3 \text{ kg per day}$). Such estimates at present still hold
45 considerable uncertainties which are discussed. Nevertheless, the results enable to place
46 constraints on the shape of the so far unknown size distribution of refractory aerosol within the
47 vortex.

48 **1 Introduction**

49 In-situ measurements of the aerosol vertical distribution inside the Arctic winter vortex of 1989
50 revealed an increase of the mixing ratios of sub-micrometer sized particles with altitude (Wilson
51 et al., 1990). Also in the Arctic (from Kiruna, Northern Sweden), in the year 2003, similar vertical
52 profiles were observed (Curtius et al., 2005) and here it was reported that an increase of particle
53 concentrations coincided with an increasing fraction of non-volatile aerosol compounds. Both
54 studies demonstrated that the abundance of particles is closely linked to air mass subsidence
55 inside the vortex from upper stratospheric or mesospheric altitudes down to the Arctic lower
56 stratosphere. Such particles provide surfaces for heterogeneous reactions and deposition of
57 condensable gases. Thus, their presence in the polar winter stratosphere may play a crucial role
58 in the formation of polar stratospheric clouds (PSC) (Voigt et al., 2005; Hoyle et al., 2013; Engel
59 et al., 2013) or in heterogeneous chemistry (Peter, 1997; Solomon, 1999; Peter and Grooß,
60 2012) connected to ozone depletion. A downward import of non-volatile particles potentially
61 occurring on a regular basis inside the vortex could imply an important natural process linked to
62 atmospheric ozone chemistry.

63 **1.1 Origin of vortex aerosol**

64 The major import of refractory aerosol material into the upper atmosphere is expected to occur
65 with the entry of meteoroids with particle diameter (d_p) smaller than 1 mm, particularly of
66 interplanetary dust particles (IDPs; $d_p < 1 \mu\text{m}$), and by the ablation of meteoroids penetrating
67 the atmosphere (von Zahn, 2005). Results from single particle chemical analyses of aerosols
68 with diameters of 300 nm - 1 μm in the Upper Troposphere/Lowermost Stratosphere (UT/LS) at
69 mid-latitudes and in the tropics suggest meteoritic ablation material is included in a large
70 fraction of stratospheric particles (Murphy et al., 2013, and references therein). The total mass
71 flux of meteoritic material into the atmosphere is estimated by various studies with different
72 approaches. These estimates range from less than 20×10^3 kg per day (Plane, 2004) to fluxes
73 between 20×10^3 kg and 100×10^3 kg per day (Cziczo et al., 2001; Gabrielli et al., 2004) and to
74 $110 \pm 55 \times 10^3$ kg per day (Love and Brownlee, 1993; Peucker-Ehrenbrink, 1996). The last value
75 currently seems to be the most accepted according to detailed discussions by von Zahn (2005).
76 Plane (2012) presents a detailed discussion of these fluxes concerning plausibility and
77 consistence with observations, and he limits the uncertainty in the flux estimates provided in the
78 literature to a factor of 10 in the order of magnitude between ~ 10 to 100×10^3 kg per day.

79 A certain fraction of this total daily influx is assumed to experience little or no ablation because
80 the meteoritic bodies are too small. With a mass below 10^{-11} kg their sizes are usually smaller
81 than 20 μm in diameter (Jones and Kaiser, 1966). Such small objects denoted as IDPs are not
82 sufficiently heated by friction with atmospheric air molecules when entering the atmosphere.
83 For large meteoroid masses ($> 100 \times 10^3$ kg and $d_p > 4$ m) the number of atmosphere-hitting
84 events of about one per year (von Zahn, 2005) is too small to significantly contribute to the total
85 influx of meteoritic material. Furthermore, von Zahn (2005) estimated that objects in the mass
86 range of 10^{-11} to 10^{-5} kg correspondent to diameters of 20 μm - 2 mm contribute the major part
87 of the total influx. These predominantly sub-millimeter sized particles are nearly fully vaporized
88 mainly in the altitude range between 75 - 120 km (Megner et al., 2008). The ablation process is
89 assumed to release atomic metal vapors that re-condense to form nanometer sized, long-lived
90 meteoritic smoke particles (MSPs) (Hunten et al., 1980; Kalashnikova et al., 2000; Plane, 2004).
91 Experimental studies provided evidence for the presence of meteoritic ablation material in the
92 mesosphere (Rapp et al., 2007; Rapp and Strelnikova, 2009; Strelnikova et al., 2009). The size of
93 MSPs may range from clusters of molecules with diameters of about 1 nm to a few hundred

94 nanometers. Numerical studies investigate the processing and transport of the initially ultrafine
95 ($d_p < 10$ nm) refractory MSPs along their atmospheric residence (Bardeen et al., 2008; Megner et
96 al., 2008; Dhomse et al., 2013). These studies also include MSP coagulation which forms larger
97 particles (secondary cosmic aerosols with $d_p > 10$ nm) as well as sedimentation and deposition
98 processes that remove the MSPs. Laboratory as well as modelling studies particularly investigate
99 the potential of MSPs to act as condensation surfaces for sulfuric acid (H_2SO_4) (Saunders et al.,
100 2010) and their impact on stratospheric H_2SO_4 processing on global scales (Saunders et al.,
101 2012). The size distribution of secondary cosmic aerosols overlaps with the size distribution of
102 IDPs that enter the atmosphere without strong thermal alteration. As a result, the size
103 distribution of refractory aerosol in the upper atmosphere is expected to be restricted to the
104 particle diameter range of 1 nm to 20 μm . Particles with diameter larger than 1 μm undergo
105 relatively fast removal due to sedimentation. The meteoritic influx is supposedly a continuous
106 process, consequently it can be assumed that sedimentation of the larger particles through the
107 region of our measurements is continuously occurring, ultimately resulting in stationary
108 equilibrium concentrations. Therefore, we can expect to find particles between the minimum
109 size determined by condensation/coagulation and the maximum size determined by the non-
110 ablation.

111 In the lower diameter range ($0.1 \mu m < d_p < 1 \mu m$) the particles have atmospheric residence times
112 of several months or, if even smaller, of years. The study of Dhomse et al. (2013) investigated the
113 distribution and transport of $^{238}PuO_2$ that was accidentally released at an altitude of 46 – 60 km
114 in the year 1964 due to re-entry and burn-up of a satellite power unit. The modelled distribution
115 of $^{238}PuO_2$ in the atmosphere and its deposition on the Earth's surface until 1974 suggest up to
116 10 years of atmospheric residence, in agreement with observations. Atmospheric residences of
117 the same order of magnitude can most likely be transferred to ablation material from
118 meteoroids. Once these particles enter regions in the atmosphere with saturated vapors, for
119 example of H_2SO_4 , nitric acid (HNO_3) or water (H_2O), heterogeneous condensation leads to
120 particle coating and growth, and finally their removal due to increased sedimentation speed or,
121 at some point, even incorporation in clouds. At mid-latitudes the particles are quickly removed
122 from the stratosphere, entering the troposphere by isentropic mixing induced by breaking
123 Rossby waves (Holton et al., 1995; Dhomse et al., 2013).

124 Recently published results from balloon-borne measurements in the Antarctic winter
125 stratosphere (Campbell and Deshler, 2014) suggest that new particle formation (NPF) may
126 provide an additional regional source of volatile particles in the vortex. At altitudes of 21 –
127 24 km aerosol number concentrations were found to be increased by a factor of 5 to 10
128 compared to background states concurrently with low fractions of less than 20 % of refractory
129 residuals. These measurements indicate relatively weak particle formation efficiencies
130 compared to excessive NPF events observed elsewhere in the UT/LS (e.g. Brock et al., 1995;
131 Weigel et al., 2011). Nevertheless, the comparably moderate abundance of particles most likely
132 caused by NPF in the Antarctic stratosphere (Campbell and Deshler, 2014) may last for longer
133 duration and may provide persistent fields with enhanced presence of particles and thus
134 reaction surfaces. However, above 24 km in the Antarctic winter stratosphere, large fractions of
135 non-volatile particles of up to 80 % are indicated (Campbell and Deshler, 2014). The same study
136 shows that with an averaged fraction of about 60 % of non-volatile particles the abundance of
137 refractory material in the Antarctic winter stratosphere is significantly increased compared to
138 the same altitude range at mid-latitudes.

139 **1.3 Vortex-driven downward transport**

140 The stratospheric vortex development causing large scale subsidence of air masses in the polar
141 region during winter is a very efficient vertical transport pathway over a wide range of
142 atmospheric altitudes. As the vortex-induced downward transport drives the import of non-
143 volatile particles from altitudes of the upper stratosphere or mesosphere (Curtius et al., 2005) it
144 is commonly assumed that the non-volatile particles to a large extent originate from space. Other
145 studies related to the Arctic vortex (e.g. Randall et al., 2006; Vogel et al., 2008) also show that
146 NO_x-rich air masses from the upper stratosphere and mesosphere, caused by energetic particle
147 precipitation (EPP) or solar proton events (SPEs), are transported downward in a strong, well-
148 isolated vortex. These studies support the hypothesis that the polar vortex generally acts as a
149 major driver for the descent of air from the mesosphere and upper stratosphere. Therefore, it is
150 expected that the Antarctic vortex air mass subsidence likewise supports this downward
151 transport. According to model studies of vertical vortex transport (e.g. Plumb et al., 2002) most
152 of the content of the mesosphere is ingested by the vortex towards the end of a polar winter and
153 the signatures of mesospheric air are discernible down to the vortex bottom. Balloon-borne
154 observations of carbon monoxide (CO) have traced mesospheric origin down to levels of 500 K
155 of potential temperature (see Figure 6 in Plumb et al., 2002), which is above the maximum
156 ceiling of the M-55 *Geophysica*. The mean large-scale subsidence inside the vortex apparently
157 occurs most efficiently at altitudes above 500 K. In fact, below 500 K mean diabatic subsidence is
158 typically insufficient to transport the bulk air mass from 500 K (or above) to 400 K over the
159 course of the winter (Greenblatt et al., 2002a; Werner et al., 2010). Vertical transport of
160 refractory aerosol to below 500 K may thus be mainly driven by diabatic dispersion within the
161 vortex rather than by mean diabatic subsidence. Diabatic dispersion may be understood as a
162 gradual vertical mixing resulting from differential subsidence together with horizontal mixing
163 (Plumb, 2007). This process has been found to be consistent with the development of observed
164 tracer distributions inside the Arctic vortex (Ray et al., 2002).

165 **1.3 Aerosol particle microphysics**

166 The polar winter vortices in general could act as the major drain pathway of aerosol from the
167 upper stratosphere and mesosphere towards the UT/LS, followed by material removal onto the
168 Earth's surface. If the subsidence of refractory particles was a regular feature this could play an
169 important role for heterogeneous PSC formation as these particles provide surfaces for
170 condensation (cf. Hoyle et al., 2013; Engel et al., 2013; Molleker et al., 2014). The availability of
171 reaction surfaces is of particular importance in times of volcanic quiescence when the
172 stratospheric Junge aerosol layer reaches relatively low particle concentrations, as for example
173 in 1997 six years after the Mt. Pinatubo eruption (Borrmann et al., 2000). It seems very plausible
174 that such particles support other microphysical processes, such as heterogeneous freezing,
175 although bulk freezing experiments (Biermann et al., 1996) indicate minor importance. PSCs
176 promote denitrification of the polar lower stratosphere as demonstrated for the RECONCILE
177 winter (Grooß et al., 2014, Woiwode et al. 2014, and Molleker et al. 2014). Denitrification
178 essentially contributes to ozone loss in the polar winter stratosphere (Fahey et al., 1990; Mann
179 et al., 2003; Waibel et al., 1999).

180 In this study we address the question whether the observed import of refractory particles into
181 the Arctic lower stratosphere was an exceptional event in 2003 (Curtius et al., 2005; Engel et al.,
182 2006) or rather a feature that regularly occurs in Arctic winters. Furthermore, from the vertical
183 distribution of refractory aerosol within the vortex obtained from three campaigns we derive
184 parameterizations which may be suitable for numerical simulations of heterogeneous PSC

185 formation and other aerosol related processes. Finally, we estimate the total refractory aerosol
186 mass inside the lower Arctic vortex and – by extrapolation of our in-situ measurements – assess
187 it in the context of the northern hemispheric daily mass influx of meteoritic material. Based on
188 these considerations we suggest that constraints may be placed on the size distribution of
189 refractory aerosol within the Arctic vortex which is so far unknown.

190 **2 Instruments and methods**

191 **2.1 Submicron particles**

192 Aerosol concentrations were measured by a 4-channel continuous flow condensation particle
193 counter COPAS (COndensation PARticle counting System) using a chlorofluorocarbon (FC-43) as
194 working liquid. COPAS measurements and data storage occur at a frequency of 1Hz. Three of the
195 four COPAS channels operate with different 50% detection particle diameters d_{p50} (i.e. 6 nm,
196 10 nm and 15 nm). The fourth COPAS channel (with $d_{p50} = 10$ nm) counts aerosol particles after
197 they have passed a heated sample flow line resulting in measured particle mixing ratios of non-
198 volatile (nv) or refractory particles (e.g. soot, mineral dust, metallic aerosol material, etc.). At an
199 operational temperature of 250°C and over the pressure range of 70 – 300 hPa this aerosol pre-
200 heater volatilizes more than 98 % of H₂SO₄-H₂O particles (Weigel et al., 2009).

201 The entry of the forward facing aerosol inlet of COPAS is positioned well outside the aircraft's
202 boundary layer. The inlet consists of two serial diffusors which decelerate the air from the free
203 flow to pumping velocity at near-isokinetic conditions. For stratospheric particle concentrations
204 the COPAS measurement uncertainty is about 10 % resulting from particle counting statistics
205 and uncertainties in the volume flow. The measurement characteristics of COPAS are described
206 in detail by Weigel et al. (2009) and its performance is demonstrated by several studies (Curtius
207 et al., 2005, Borrmann et al., 2010, Frey et al., 2011, Weigel et al., 2011).

208 Particle concentrations are initially measured in particle number per cubic centimeter of
209 sampled air, but are presented here as mixing ratio N in units of particles per milligram of air
210 (mg⁻¹) for comparing measurements from different pressure altitudes and for correlations with
211 tracer mixing ratios. In the following N_{10} denotes the mixing ratio of particles with diameters
212 larger than 10 nm up to about 1 μm. N_{10nv} refers to the mixing ratio of non-volatile particles in
213 the same size range. The fraction f of non-volatile particles is given as the ratio of N_{10nv} and N_{10}
214 in % as only non-volatile particles with sizes $d_p > 10$ nm are detected. The measurement of
215 particles with $d_p > 6$ nm and $d_p > 15$ nm aims in principle at the identification of recently
216 occurred NPF (cf. Weigel et al., 2011). However, throughout all measurements discussed here,
217 no such NPF event was identified.

218 **2.2 Dynamic tracer nitrous oxide**

219 Nitrous oxide (N₂O), a long-lived atmospheric tracer, is measured in-situ on board the M-55
220 *Geophysica* by the HAGAR (High Altitude Gas Analyzer) instrument (Werner et al., 2010; Homan
221 et al., 2010). N₂O is detected by gas chromatography with electron capture detection (GC/ECD)
222 along with other long-lived species like chlorofluorocarbons (CFCs), sulfur hexafluoride (SF₆)
223 and methane (CH₄) with a temporal resolution of 90 s. The mean precision for the N₂O
224 measurements, given in % of the tropospheric value (~ 320 ppb), is below 0.5 % for all three
225 campaigns, except the first four flights during EUPLEX for which it is 1-1.3 %. For most flights it
226 is in fact below 0.3 %.

227 N₂O is generated at the surface and has its sink at high altitudes, generally above the tropopause,
 228 where with increasing altitude the N₂O molecules are destroyed by UV-photo-dissociation and
 229 reaction with O (¹D), oxygen atoms in an excited singlet state. Satellite observations of episodic
 230 N₂O enhancements in the polar mesosphere (Funke et al., 2008) also suggest the presence of a
 231 minor mesospheric source. Nevertheless, from a stratospheric perspective, air masses with low
 232 N₂O mixing ratio generally originate from high altitude, i.e. in the mid to upper stratosphere or
 233 mesosphere. Air masses originally coming from the upper stratosphere and further above
 234 subside over the course of the winter within the Arctic polar vortex. This is indicated at a given
 235 altitude by N₂O mixing ratios substantially decreasing with time (Greenblatt et al., 2002a). This
 236 process is also verified and quantified by numerical studies (Prather and Rodriguez, 1988;
 237 Fisher et al., 1993; Plumb et al., 2002). Enhanced mixing ratios of carbon monoxide and
 238 molecular hydrogen coinciding with low values of SF₆ (Engel et al., 2006) indicate particularly
 239 strong downwelling of air even from the mesosphere during the 2003 EUPLEX winter (January
 240 through March).

241 Due to the strong subsidence and dynamical isolation of air inside the vortex, N₂O and other
 242 long-lived tracers exhibit sharp meridional gradients at the vortex edge. Greenblatt et al.
 243 (2002b) demonstrated that the inner edge of the Arctic vortex can be accurately determined by
 244 the excess of measured N₂O_{meas.} relative to characteristic values inside the vortex at a given
 245 potential temperature and at a given time, i.e. $\Delta N_2O = N_2O_{meas.} - N_2O_{vortex}(\Theta)$. At levels around
 246 450 K that study (Greenblatt et al., 2002b) found a ΔN_2O value of ~ 20 nmol mol⁻¹ to generally
 247 correspond well to the dynamical Nash-criterion (Nash et al., 1996) which is a commonly used
 248 criterion for defining the vortex edge. Extending this concept, we here define what we denote as
 249 the ΔN_2O vortex index (ξ_{vi}) as:

$$250 \quad \xi_{vi} = 1 - \frac{\Delta N_2O(\Theta)}{N_2O_{mid-lat.}(\Theta) - N_2O_{vortex}(\Theta)} \quad (1)$$

251 Essentially, the N₂O mixing ratios are linearly rescaled to altitude-independent characteristic
 252 index values of $\xi_{vi} = 1$ inside the vortex, and $\xi_{vi} = 0$ at mid-latitudes. This vortex index will be
 253 introduced and evaluated in detail in a further study (Hösen et al., 2014), which will also
 254 demonstrate that ξ_{vi} can, with some caveats, be viewed as an empirical proxy for the fraction of
 255 vortex air in an observed air mass. As the vortex index is conserved on time scales of isentropic
 256 transport, it essentially provides information on whether a measured air mass originally came
 257 from the interior of the vortex or from the outside. Therefore, the COPAS measurements can be
 258 categorized with respect to their recent origin by means of the index ξ_{vi} . The theoretically
 259 maximum value of ξ_{vi} is one, indicative of pristine vortex air mass. The criterion limits defined
 260 for this study to classify the COPAS measurements for Θ -levels above 400 K are:

- 261 1) $\xi_{vi} > 0.75$: Sample air originating primarily from the vortex interior,
- 262 2) $0.75 < \xi_{vi} < 0.25$: Sample air with extra-vortex, mid-latitude air contributions which are too
 263 large for unambiguous apportioning.
- 264 3) $\xi_{vi} < 0.25$: Sample air originating from well outside of the polar vortex,
 265 consisting mostly of mid-latitude air.

266 Since the ξ_{vi} -range between 0.4 and 0.8 is populated by relatively few air samples mostly
 267 originating from the vortex edge region, the resulting selection of vortex and extra-vortex data
 268 mainly needed in this study (i.e. categories 1) and 3)) is fairly insensitive to the exact choice of
 269 the criterion limits.

270 The COPAS measurements are recorded with 1Hz temporal resolution. One single N₂O data point
271 is measured by HAGAR only once every 90 seconds, representative for the air sampled during 2-
272 3 seconds. Consequently, the vortex index ξ_{vi} has the same temporal resolution. Each ξ_{vi} value is
273 associated with five COPAS readings, extending from two seconds before the HAGAR
274 measurement point to two seconds after. This approach compensates a possible offset of about 1
275 second between the controller clocks of COPAS and HAGAR. Those COPAS measurements which
276 are not attributable to a value of N₂O mixing ratio or vortex index are excluded from the analysis.
277 The results of the COPAS measurements from EUPLEX (2003) were already discussed in detail
278 by Curtius et al. (2005). However, that study apportioned the data records to the vortex interior
279 or exterior by means of the chemistry transport model CLaMS (see also Section 2.4). The results
280 from 2003 discussed here are re-calculated adopting the empirical measure of ξ_{vi} based on in-
281 situ observations during EUPLEX. Consequently, the analysis of EUPLEX data here is based on a
282 different approach, though the conclusions from this re-calculation do not differ from the
283 interpretation of Curtius et al. (2005).

284 **2.3 Meteorological measurements**

285 Ambient air temperature and static pressure were measured with the Thermo Dynamic Complex
286 (TDC) probe with 1 Hz resolution and an accuracy of 0.5 K (Shur et al., 2007). If TDC data were
287 not available (e.g. throughout ESSenCe) temperature and pressure data were adopted from the
288 Unit for Connection with the Scientific Equipment (UCSE, Sokolov and Lepuchov, 1998), a part of
289 the navigational system of the M-55 *Geophysica*. UCSE data are provided as 1 Hz-resolved
290 ambient pressure (with an accuracy of ± 1 hPa) and temperature (± 2 K accuracy).

291 **2.4 CLaMS modelling**

292 Model simulations with the 3-dimensional Chemistry Transport Model (CLaMS) (McKenna et al.,
293 2002a; McKenna et al., 2002b; Konopka et al., 2007; Grooß et al., 2014) were performed with
294 extensive stratospheric chemistry, including heterogeneous chemistry and particle
295 sedimentation, driven by ERA-Interim reanalysis data for the EUPLEX, RECONCILE and ESSenCe
296 campaigns. For all simulations a suite of inert artificial tracers was utilized, which mark
297 particular regions in the atmosphere (e.g. vortex air and mid-latitude air according to the Nash-
298 criterion) at the beginning of each simulation. The advection and mixing of the marked air
299 parcels is then modelled by the CLaMS transport scheme, which allows the tracking of the air
300 mass and the detection of its origin (Günther et al., 2008) covering the northern hemisphere. For
301 EUPLEX and RECONCILE the CLaMS simulations were conducted with a horizontal resolution of
302 approximately 70 km and a maximum vertical resolution of about 400 m around the tropopause.
303 The simulations were initialized at the beginning of the winter, usually on 01 December, using
304 satellite measurements and tracer-tracer correlations following Grooß et al. (2014). For
305 ESSenCe the CLaMS simulations were initialized on 01 November 2011 and yielded a horizontal
306 resolution of 100 km. For our study an analysis of the tracer distributions led to the
307 determination of the horizontal vortex cross section area (VCSA) averaged for the respective
308 campaign. The VCSAs were calculated within the altitude range that was covered by the in-situ
309 measurements, i.e. between 400 K and 500 K of potential temperature. For this altitude range
310 the VCSA is obtained by means of CLaMS calculations in Θ -steps of 10 K as a mean value ± 5 K.
311 The calculated VCSAs exclude any air recently intruded from mid-latitudes for which the
312 selected observations would not be representative.

313

314 **2.5 Total mass of refractory aerosol matter**

315 The total refractory aerosol mass within the investigated altitude range ($400 \text{ K} < \theta < 500 \text{ K}$)
316 inside the vortex is estimated in principle by (a) subdividing the vortex column into 10 layers,
317 each of $\Delta\theta = 10 \text{ K}$ thickness, (b) calculating the total mass of the refractory aerosol from the
318 measured $N_{10\text{nv}}$ as a function of θ inside each VCSA-layer, assuming certain particle number size
319 distributions which are converted into volume/mass distributions, and (c) adding up the aerosol
320 masses of all layers. In more detail, our estimates are based on parameterizations of the in-situ
321 measurements (cf. Section 6) and on the following assumptions:

322 (1.) Inside the vortex the refractory aerosol mixing ratio that is parameterized as a function of θ
323 is assumed to be constant across the surface of each VCSA level. Furthermore, the values are
324 assumed to be time-invariant during the relatively short campaign periods of 3-4 weeks.

325 (2.) The size distribution of the refractory aerosol material is assumed to be constant.
326 Furthermore, the size distribution is expected to be within a range that has (a.) as uppermost
327 limit: three different parameterizations of the stratospheric background aerosol (Jaenicke, 1980,
328 Wang et al., 1989, and Deshler, 2008) and (b.) as lowermost limit: the numerically modelled size
329 distribution of MSPs that have reached 30 km altitude over the winter pole (Bardeen et al.,
330 2008) (cf. Figure 1). The integrals over the respective model size distributions are scaled such
331 that they represent the absolute values of observed $N_{10\text{nv}}$. Note that an individual stratospheric
332 sulfuric acid particle may incorporate more than one refractory core. The COPAS technique does
333 not unambiguously allow for assorting an individual refractory residual to a single sulfuric acid
334 droplet. It also does not allow for a strict conclusion as to whether multiple refractory
335 incorporations adhere together after the volatile aerosol compounds are vaporized due to the
336 heated COPAS aerosol line. We assume, however, that after contraction due to the surface
337 tension of each evaporating droplet, the van-der-Waals forces will keep the remaining refractory
338 residuals in shape of a single particle.

339 (3.) The particle's material density ρ_p is estimated to be on average about 2000 kg m^{-3} , with an
340 uncertainty range of $1000 - 3000 \text{ kg m}^{-3}$. The chosen average value is in general agreement with
341 former studies where ρ_p of 2000 kg m^{-3} was used, referring to the density of a typical stone
342 meteorite (Chondrite, e.g. Hunten et al., 1980 or Plane, 2004). We use ρ_p of 3000 kg m^{-3} as the
343 uppermost limit as this accounts for the possibility that chemical conversion of meteoritic
344 material dissolved in the H_2SO_4 liquid phase produces salts such as iron sulfate hydrates.

345 (4.) To estimate the particle burden as a function of model pressure altitude the relationship
346 between the potential temperature θ (in K) and the atmospheric pressure p (in hPa) is needed
347 which is derived from parameterizations of the measured values of θ and p .

348 **3 Field campaigns in the years 2003, 2010 and 2011**

349 Three measurement campaigns were carried out in the Arctic winter seasons of the years 2003,
350 2010 and 2011, from Kiruna, Northern Sweden ($67^\circ 49' \text{ N}$, $20^\circ 30' \text{ E}$) deploying the high altitude
351 research aircraft M-55 *Geophysica* (Stefanutti et al., 1999), which is capable of operating at
352 altitudes of up to 20 km:

353 (1.) EUPLEX, January – March 2003: 15 mission flights

- 354 • *EUropean Polar stratospheric cloud and Lee wave EXperiment* (Günther et al.,
355 2008)

- 356 • combined with the European space agency (ESA) ENVISAT – Arctic Validation
357 Campaign,
358 (2.) RECONCILE, January – March 2010: 13 mission flights
359 • *Reconciliation of essential process parameters for an enhanced predictability of*
360 *Arctic stratospheric ozone loss and its climate interactions* (von Hobe et al., 2013).
361 • completed by a two-flight mission PremierEX (Spang et al., 2012) and
362 (3.) ESSenCe (ESa Sounder Campaign), December 2011: 2 mission flights (Kaufmann et al.,
363 2014).

364 **3.1 EUPLEX**

365 The flight activities during EUPLEX/ENVISAT-validation (in the following EUPLEX) took place
366 between 10 January through 19 March 2003 with a downtime between 11 and 28 February.
367 Stratospheric air mass exchange between the interior and exterior of the polar vortex during
368 EUPLEX was analyzed by Günther et al. (2008) and further discussed by Werner et al. (2010). In
369 summary, two major vortex break-up events happened during the EUPLEX period: (a.) from 21
370 January through 23 January, and (b.) from 15 February to 23 February. Both were followed by
371 vortex recombination (Günther et al., 2008).

372 **3.2 RECONCILE and PremierEX**

373 The flight activities during RECONCILE/PremierEX (abbreviated as RECONCILE) were
374 conducted between 17 January and 10 March 2010. During RECONCILE there was a downtime
375 between 02 and 27 February (cf. von Hobe et al., 2013). As described by Dörnbrack et al. (2012),
376 the polar vortex disintegrated into two parts around 15 December 2009 just prior to the
377 RECONCILE flight operations and recombined around 25 December 2009. A second vortex
378 break-up occurred in mid-February followed by recombination in early March. During both
379 break-up events the coldest of the two vortex fragments survived and regenerated. The
380 regeneration period to recover a compact vortex structure lasted until the beginning of January
381 2010 and the beginning of March 2010, respectively. The simulation of inert artificial tracers in
382 the CLaMS model indicates that the first vortex split in December 2009 caused a strong exchange
383 and dilution of air inside the vortex with air from lower latitudes. In contrast, the second split of
384 the vortex negligibly influenced the air composition inside the vortex. After regeneration at the
385 beginning of March 2010 the air chemical composition inside the vortex exhibited a high grade
386 of homogenization compared to the conditions found following the first split of the vortex in
387 December 2009.

388 Both missions, EUPLEX and RECONCILE, covered the same seasonal time in the Arctic winter
389 and early spring period. For EUPLEX and RECONCILE the data of the first and second phases,
390 before and after the downtimes, are denoted with suffixes -A and -B.

391 **3.3 ESSenCe**

392 The flight activities during ESSenCe were performed during December of 2011, i.e. early in the
393 winter season. In contrast to the more disturbed and warm Arctic winters of 2002/03 and
394 2009/10, the vortex during ESSenCe remained mainly unperturbed. The absence of perturbation
395 led to the early formation of a strong horizontal transport barrier and very cold temperatures
396 below 192 K at the 50 hPa pressure level in December 2011. During the ESSenCe winter
397 extended fields of persisting synoptic scale PSCs were observed and probed (Molleker et al.,
398 2014; Woiwode et al., 2014).

399 **4 Observations and results**

400 The measured aerosol mixing ratios in the Arctic winter stratosphere are summarized in Figure
401 2 through Figure 4.

402 **4.1 EUPLEX winter 2003**

403 **Outside the polar vortex ($\xi_{vi} < 0.25$):** For $\Theta > 400$ K the mixing ratio N_{10} remains fairly
404 constant (150 - 300 mg⁻¹) and slightly decreases down to 200 mg⁻¹ with increasing Θ until 440 K
405 (Figure 2). The fraction f of non-volatile particles (Figure 2c) for EUPLEX-A generally remains
406 below 50 %.

407 **Variable mixing states of vortex air with mid-latitude air ($0.25 < \xi_{vi} < 0.75$):** N_{10} is usually
408 constrained to lower values between 100 - 200 mg⁻¹. For variable mixing stages the values of f
409 range between 25-60 %.

410 **Inside the vortex ($\xi_{vi} > 0.75$):** N_{10} continuously increases with Θ . This is particularly obvious in
411 Figure 2a from the vertical profile of N_{10} for the EUPLEX-A period. Also, during EUPLEX-A the
412 mixing ratio of non-volatile particles N_{10nv} behaves similarly as a function of altitude (Figure
413 2b). Inside the polar vortex N_{10nv} increases considerably with rising Θ , and significantly exceeds
414 the magnitude of N_{10nv} observed outside the vortex. The fraction f is generally larger than 50 %
415 and reaches up to 80 % during EUPLEX-A.

416 For EUPLEX-B (Figure 2d) the vertical dependence of N_{10} in principle behaves similarly to the
417 EUPLEX-A period. However, despite the fact that the M-55 *Geophysica* operated at its maximum
418 ceiling, the high Θ -levels of EUPLEX-A could not be reached during EUPLEX-B. Nevertheless,
419 N_{10nv} from Figure 2e resembles the observations of EUPLEX-A. While differences in f between
420 the inside and the outside of the vortex are visible in both data sets, the highest values of up to
421 80 % were measured during EUPLEX-A.

422 **4.2 RECONCILE winter 2010**

423 **Outside the polar vortex ($\xi_{vi} < 0.25$):** During RECONCILE-A N_{10} does not significantly differ
424 between the inside and the outside of the vortex (Figure 3a). In RECONCILE-B, the
425 measurements were mainly made outside the polar vortex with the highest Θ -levels above
426 510 K. Here N_{10} (Figure 3d) shows a nearly constant profile with values at about 100 mg⁻¹ for
427 $\Theta > 400$ K.

428 **Inside the vortex ($\xi_{vi} > 0.75$):** The vertical profile of N_{10nv} (Figure 3b) indicates that the mixing
429 ratio of refractory aerosol increases inside the vortex where also the highest values of the
430 fraction f (Figure 3c) are reached. During RECONCILE-A the inside and outside vortex
431 distributions are clearly less distinct compared to EUPLEX. This lack of contrast could be due to
432 significant dilution of the vortex content with mid-latitude air associated with the vortex break-
433 up and recombination prior to RECONCILE-A. Only a few measurements could be performed
434 well inside the polar vortex during RECONCILE-B. These show in contrast to RECONCILE-A a
435 considerable increase in N_{10nv} from about 80 mg⁻¹ to nearly 180 mg⁻¹ between 400 K and 460 K.

436 **4.3 ESSenCe winter 2011**

437 **Outside the polar vortex ($\xi_{vi} < 0.25$):** Compared to EUPLEX and RECONCILE, the particle
438 mixing ratios measured during ESSenCe in December 2011 are generally low (Figure 4a) with
439 values of N_{10} smaller than 100 mg⁻¹ for $\Theta > 400$ K.

440 **Inside the vortex ($\xi_{vi} > 0.75$):** The vertical profile of N_{10nv} (Figure 4b) exhibits a steeper
441 increase with altitude than N_{10} which agrees qualitatively with corresponding results of the
442 previous campaigns. As a consequence, similarly high values of f are found (Figure 4c). This
443 means that during ESSenCe the highest fractions of f were also observed inside the polar vortex
444 reaching values between 60 % and 80 %.

445 **5 Synopsis of observations during individual Arctic winters**

446 All observed vertical profiles of the submicron particle mixing ratios are compared in Figure 5 in
447 terms of medians with percentiles:

448 **5.1 Outside the polar vortex ($\Theta > 400$ K)**

449 **N_{10} :** Lowest values of N_{10} at all altitudes are reached in the earliest winter period (ESSenCe,
450 Figure 5a). Later in the winter N_{10} may either remain nearly constant with altitude (RECONCILE,
451 Figure 5i) or may exhibit variability, reaching an enhancement by a factor of up to 2.5 during
452 EUPLEX (Figure 5e). The considerable difference in the vertical distribution of N_{10} between the
453 EUPLEX A- and B- periods (between 430 – 450 K) may be related to an air mass exchange with
454 vortex air during the vortex break-up (Curtius et al., 2005, Werner et al., 2010).

455 **N_{10nv} :** Values of N_{10nv} are similar with 30 - 50 mg^{-1} for all late-winter situations (Figure 5f and
456 j). In contrast, during early winter, the values are between 20 - 35 mg^{-1} , and thus lower (Figure
457 5b).

458 **Fraction f :** Isentropic air mass exchanged prior to EUPLEX-B is also indicated by the decreased f
459 (Figure 5h, open red circles) for $\Theta > 420$ K. In general, values for f of 25 - 50 % are very similar
460 for ESSenCe (Figure 5d) and EUPLEX (Figure 5h). During RECONCILE (Figure 5i) f is generally
461 higher, reaching 50 % for $\Theta < 450$ K. Further above ($450 \text{ K} < \Theta < 510 \text{ K}$) f is increasing up to
462 60 % outside the polar vortex.

463 However, high Θ -levels ($450 \text{ K} < \Theta < 510 \text{ K}$) were only reached outside the vortex during the
464 second winter period of the year 2010 (RECONCILE-B) and comparable data are not available
465 from the other campaigns.

466 **5.2 Inside the polar vortex ($\Theta > 400$ K)**

467 **N_{10} and N_{10nv} :** Both mixing ratios exhibit a considerably steeper increase with Θ than found
468 outside the vortex. Additionally, the gradient of the enhancement of $N_{10nv}(\Theta)$ is stronger than
469 for $N_{10}(\Theta)$. Differences between the A- and B- phases of EUPLEX and RECONCILE result mainly
470 from the air mass descent within the vortex. Although N_{10} is comparably low during ESSenCe
471 (Figure 5a), also here the increase of $N_{10nv}(\Theta)$ (Figure 5b) is steeper than that of $N_{10}(\Theta)$.

472 **Fraction f :** The strongest increase of f with Θ were observed (a.) for EUPLEX-A, RECONCILE-B –
473 with less disturbed vortex conditions for a certain period prior to the observations and (b.)
474 during ESSenCe when the vortex had just developed. Values of f as high as 70 % were found in
475 the vortex at $\Theta \sim 450$ K. Only for EUPLEX-A and RECONCILE-B the median values exceed 70 % at
476 higher altitudes (~ 470 K in RECONCILE-B, Figure 5i). In the Θ -range above 480 K only data
477 from EUPLEX-A indicate a slight decrease of f with increasing potential temperature.

478 **5.3 Contribution of volatile particles**

479 With the mixing ratio difference given as $N_{10} - N_{10nv}$ the contribution of volatile and semi-volatile
480 particles is accounted for. As long as coated non-volatile particles have diameters larger than
481 10 nm they are included in N_{10} . Once the volatile coating is removed, releasing a residual with

482 $d_p < 10$ nm, this remnant is not accounted for with N_{10nv} . Therefore, the COPAS measurement
483 technique does not allow for distinguishing between either a fully volatile particle or a semi-
484 volatile particle with a diameter of close to 10 nm. The mixing ratio difference $N_{10}-N_{10nv}$ during
485 ESSenCe (Figure 5c) decreases for $\Theta > 400$ K outside the vortex and remains nearly constant as a
486 function of altitude inside the vortex. For EUPLEX (Figure 5g) $N_{10}-N_{10nv}$ does not exhibit such a
487 steep increase with altitude inside the vortex as found for N_{10nv} . Surprisingly, for the
488 RECONCILE case (Figure 5k) very similar values of $N_{10}-N_{10nv}$ with Θ are measured inside and
489 outside of the vortex as well as during RECONCILE-A and RECONCILE-B. The most likely reason
490 for this is inherent in the vortex instability. During RECONCILE the vortex was more disturbed
491 and inhomogeneous than during EUPLEX or ESSenCe (cf. Section 3).

492 In summary, increasing particle mixing ratios inside the Arctic vortex are mainly due to
493 refractory aerosols increasing with altitude. The fact that N_{10nv} and $N_{10}-N_{10nv}$ behave differently
494 indicates that N_{10nv} has sources that are decoupled from those of the mainly volatile aerosols.
495 Essentially, the constant values of $N_{10}-N_{10nv}$ observed inside and outside the vortex over the
496 complete RECONCILE mission period may be a result of exceptionally warm stratospheric
497 temperatures. However, for the RECONCILE case this means:

498 (a.) Increasing particle mixing ratios as a function of altitude inside the vortex are primarily
499 supplied by aerosol containing refractory cores. Otherwise, $N_{10}-N_{10nv}$ would generally show a
500 similar increase with altitude, and

501 (b.) Even if $N_{10}-N_{10nv}$ includes non-volatile residuals too small to be detected ($d_p < 10$ nm), the
502 particles descending inside the vortex during RECONCILE consisted predominantly of non-
503 volatile particles larger than 10 nm.

504 **5.4 Particle mixing ratio as function of N₂O mixing ratio**

505 In Figure 6 the particle mixing ratios N_{10nv} and the fractions f are correlated with the mixing
506 ratio of the long-lived tracer N₂O which was concurrently measured. Since the N₂O mixing ratios
507 monotonically decrease with rising altitude in the stratosphere, the ordinates in Figure 6 are
508 reversed.

509 For high N₂O mixing ratios (> 250 nmol mol⁻¹) positive correlations are found as N₂O as well as
510 N_{10nv} and f decrease with altitude in the lowermost stratosphere. At smaller N₂O mixing ratios
511 there is no or only a slight anticorrelation, i.e. increasing N_{10nv} and f with decreasing N₂O mixing
512 ratios. At values of N₂O below 200 nmol mol⁻¹ (i.e. at values typical for the Arctic lower
513 stratosphere) a clear anticorrelation is observed showing rising N_{10nv} and f with decreasing
514 N₂O. These low N₂O values (down to 70 nmol mol⁻¹) indicate that air masses from higher
515 altitudes descended inside the vortex. The elevated concentrations of refractory particles are
516 thus an indication of such non-volatile materials being supplied from aloft. As this
517 anticorrelation is very similar for the late-winter campaigns of EUPLEX and RECONCILE, its
518 occurrence apparently is not a unique event. Unfortunately for ESSenCe no flights were
519 conducted in the late winter season.

520 Inside the vortex the mixing ratio N_{10nv} generally increases faster than N_{10} with decreasing N₂O.
521 As a consequence, the fraction f of non-volatile particles grows with altitude and falling N₂O, and
522 refractory aerosol particles increasingly contribute to the enhanced particle mixing ratios. The
523 ratio f is shown in Figure 6f through Figure 6j as a function of the N₂O mixing ratio. For N₂O
524 mixing ratios below 175 nmol mol⁻¹, the fraction of non-volatile aerosol is about 50 %, or higher.

525 Further above f increases to values of up to 80 % (EUPLEX-A - Figure 6g, RECONCILE-B - Figure
526 6j or ESSenCe - Figure 6f). Contrary to N_{10nv} the gradients of the fraction f with decreasing N_{2O}
527 seem to compare well throughout all cases. This includes the measurements from ESSenCe as
528 well and appears to be independent of the progress of the respective winter season.

529 In summary, the observations reveal that inside the polar vortex and above 490 K potential
530 temperature up to 150 mg^{-1} (N_{10nv}) from a total of 200 mg^{-1} (N_{10}) are thermally stable at 250°C .
531 Therefore, a large fraction of investigated aerosols does not evaporate at 250°C and contains
532 materials other than H_2SO_4 , HNO_3 , H_2O or other volatile compounds. For these reasons it can be
533 assumed that the thermo-stable aerosols are predominantly comprised of meteoric ablation
534 materials, although detailed chemical analyses of such particles in the submicron size range are
535 still scarce (cf. Murphy et al., 2013 and references therein).

536 6 Implication of the observations and discussion

537 6.1 Vertical profiles of non-volatile particle mixing ratio

538 The study of Wilson et al. (1990) already described increasing submicron aerosol concentrations
539 at altitudes of up to 20 km inside the Arctic vortex by measurements utilizing the NASA *ER-2*
540 aircraft during the Airborne Arctic Stratospheric Expedition (AASE) in January and February
541 1989. Further evidence for an increasing number concentration of condensation nuclei (CN) as a
542 function of altitude was found from balloon-borne measurements with significant excess at
543 higher altitudes (between 20 - 28 km) at Kiruna in January 1990 (Hofmann et al., 1990, Figure
544 1a therein). However, Wilson et al. (1990) suggested that homogeneous nucleation of the
545 $\text{H}_2\text{SO}_4/\text{H}_2\text{O}$ system may have been the source of these particles in the Arctic winter stratosphere.
546 The observations of Campbell and Deshler (2014) in the Antarctic vortex seem to support this
547 suggestion.

548 Nevertheless, recent new particle formation was never identified throughout our Arctic
549 measurements as increased concentrations of ultrafine particles (with $6 \text{ nm} < d_p < 15 \text{ nm}$) were
550 not observed. In addition, the particle mixing ratio difference $N_{10}-N_{10nv}$ (Figure 5) remains fairly
551 constant with altitude inside and outside the vortex (ESSenCe, Figure 5c, RECONCILE Figure 5k).
552 However, if $N_{10}-N_{10nv}$ increases with altitude then N_{10nv} increases more strongly (EUPLEX,
553 Figure 5f and Figure 5g) particularly inside the vortex. Thus, it seems apparent that enhanced
554 particle mixing ratios with altitude are mainly linked to a supply of refractory particles from
555 higher altitudes.

556 Of course, it cannot be ruled out that many refractory residuals were too small (if $d_p < 10 \text{ nm}$) to
557 be detected with COPAS. Such ultrafine particles are produced by re-condensation of metallic
558 vapors from meteoritic ablation to form MSPs (Megner et al. 2008; Saunders et al., 2012;
559 Dohmse et al., 2013). Particles in this size range, for instance if involved in noctilucent cloud
560 formation, could be transported down to the middle stratosphere. Plane, (2012) suggests by
561 referring to numerical studies (Bardeen et al., 2008; and Megner et al., 2008) that these ultrafine
562 particles most likely agglomerate to diameters of up to 80 nm, e.g. driven by electrical charges,
563 before entering the middle stratosphere from above. It is possible that the observations made by
564 Wilson et al. (1990) also included a major fraction of refractory aerosol material. Under this
565 assumption, and considering the observations by Curtius et al. (2005) from EUPLEX together
566 with our findings presented in this study, we hypothesize that this particle import is a regular
567 feature of the late winter polar vortex in the Northern hemisphere, provided that the vortex
568 develops throughout the season without being strongly diluted by mid-latitude in-mixing.

569 **6.2 Correlations of non-volatile particles with tracer N₂O**

570 As shown in Figure 6a through Figure 6e the enhancement of refractory aerosol particles larger
571 than 10 nm with decreasing N₂O inside the vortex results in a rather compact anticorrelation.
572 This correlation of N_{10nv} and N₂O is indicated by the linear fits for data points with ξ_{vi} higher
573 than 0.75. The slope of the correlation is much smaller for the ESSenCe period in December 2011
574 (Figure 6a) than for the other cases, and the steepest slopes are found for the EUPLEX-B and
575 RECONCILE-B periods in late winter.

576 The observed correlations between N_{10nv} and the long-lived tracer N₂O can be consistently
577 interpreted in terms of the theory of stratospheric tracer-tracer correlations which is well
578 developed and verified by observations (cf. Plumb, 2007, and references therein).

579 In the absence of the polar vortex, rapid isentropic mixing creates a unique extra-tropical
580 canonical correlation between two long-lived tracers. The shape of the canonical correlation of
581 tracers is determined by the vertical distribution of the respective sources and sinks. In
582 particular, this canonical correlation is expected to exhibit curvature in the region close to sinks
583 or to sources of either compound, but to be linear elsewhere.

584 After the formation and ensuing subsidence of the polar vortex the polar transport barrier
585 isolates the air inside the vortex. As a consequence the correlation within the vortex may change
586 over the course of the winter due to diabatic dispersion within the vortex and/or in-mixing of
587 mid-latitude air. For reasons explained in Plumb (2007) the effect of these processes is a
588 progressive straightening of the correlations. Thus, while the curved canonical correlation is
589 expected to remain almost unchanged at mid-latitudes, the correlation inside the vortex is
590 expected to progressively deviate from the canonical curve toward its concave side due to
591 diabatic dispersion and/or mid-latitude in-mixing.

592 The grey lines in Figure 6 are congruent with the ESSenCE correlation inside the vortex,
593 qualitatively extrapolated by its expected continuation toward lower N₂O values. Above the
594 sampled altitudes N₂O continues to decline and eventually converges towards zero in the
595 mesosphere while N_{10nv} will further increase by approaching the source region of the refractory
596 aerosol. The observed evolution of the correlations inside the vortex toward higher N_{10nv} at a
597 given N₂O from early winter (ESSenCE, Figure 6a), to mid and late winter (EUPLEX: Figure 6b or
598 RECONCILE: Figure 6e) corresponds indeed to a progressive deviation toward the concave side
599 of the original curve as expected according to the arguments of Plumb (2007) described above.

600 Note that the correlations cannot change due to the mean large-scale subsidence. The
601 correlations could only deviate from their canonical shape due to diabatic dispersion and/or in-
602 mixing from mid-latitudes (cf. Plumb, 2007). However, these processes, dispersion or in-mixing,
603 would have different effects on the evolution of the vertical profiles. (1) Mid-latitude in-mixing
604 would tend to decrease particle mixing ratios at a given potential temperature above 410 K, thus
605 counteracting the mean subsidence. (2) Alternatively, diabatic dispersion would lead to
606 additional dispersive downward transport of particles. Because of the observed strong particle
607 increase at all potential temperatures above 410 K between early and late winter (despite slow
608 mean subsidence at these altitudes), we hypothesize that:

- 609 1) The diabatic dispersion is the dominant factor in the evolution of the correlations and
610 likely also contributes significantly to the evolution of the vertical profiles.

611 2) The diabatic dispersion is thus an important mechanism for the transport of refractory
612 particles to the vortex bottom.

613 In order to evaluate similarities and differences of the gradient as a function of Θ and the N_2O
614 mixing ratio Figure 7 shows the corresponding scatter plots. Note that only measurement points
615 from the vortex interior are displayed and that the scale of the color code extends from 0.75 to
616 1.0 for ξ_{vi} .

617 **6.2.1 Outflow region at the vortex bottom ($380\text{ K} < \Theta \leq 410\text{ K}$)**

618 From the RECONCILE data set shown in Figure 7b and Figure 7e it can be seen that the functions
619 $N_{10nv}(\Theta)$ and $N_{10nv}(N_2O)$ are not linear over the entire range of Θ and N_2O . Instead there is a
620 much smoother increase for $380\text{ K} < \Theta \leq 410\text{ K}$ compared to $\Theta > 410\text{ K}$. The data points of the
621 altitude range below 410 K are shown as crosses (Figure 7b), likewise for the EUPLEX (Figure
622 7a) and ESSenCe (Figure 7c) data. The deviation from a single straight line is most pronounced
623 for RECONCILE. For ESSenCe, there may not have been enough data points or, more likely, the
624 distinct gradients for altitudes above 410 K had not yet developed during early winter.

625 The two different correlations of the two altitude bands may arise from the dynamics at the
626 vortex bottom. Below 410 K (Figure 7b), the vortex boundary no longer acts as an effective
627 transport barrier, thus allowing for more efficient isentropic exchange and mixing with the mid-
628 latitudes (Haynes and Shuckburgh, 2000). As a result, in this region, no separate vortex
629 correlation forms. Observational indications for the existence of such a transition zone were
630 previously described by Weinheimer et al. (1993). For a very similar Θ -altitude range Borrmann
631 et al. (1995) identified this transition zone below the vortex bottom by linear correlations
632 between ozone and the aerosol surface area mixing ratio, though from larger particles of
633 volcanic origin. The described discontinuity is not only present in the linear correlations
634 between the mixing ratio N_{10nv} and potential temperature, but also in those between N_{10nv} and
635 N_2O for RECONCILE (Figure 7e). This clearly shows that different air masses are involved, and
636 we presume that efficient air mass exchange in the outflow region at the vortex bottom causes
637 the observed discontinuity. A similar although much less pronounced discontinuity is also
638 observed for ESSenCe, while for EUPLEX there are too few observations at the vortex bottom for
639 it to be discerned.

640 **6.2.2 In the unperturbed vortex ($\Theta > 410\text{ K}$)**

641 The plots in Figure 7 exhibit linear relationships over most of the observed N_2O -range with
642 correlation coefficients r^2 of 0.72-0.90 for EUPLEX, RECONCILE and ESSenCe (cf. Table 1). Over
643 the observed Θ -range the r^2 of 0.54 for the ESSenCe case indicates comparably weak confidence
644 in a linear relationship between Θ and N_{10nv} .

645 All linear regressions of N_{10nv} versus the potential temperature and the N_2O mixing ratio from
646 the three field campaigns are shown for comparison in Figure 8, together with the 95 %-
647 confidence intervals. The resulting regression parameters are presented in Table 1.

648 (a.) N_{10nv} as a function of potential temperature (Figure 8a):

649 $N_{10nv}(\Theta)$ strongly depends on the large-scale dynamics of the vortex, in particular on the
650 strength of vortex descent and on the vortex stability over the winter period. The observed
651 vertical gradients of the three campaigns are qualitatively consistent with continuing diabatic
652 descent of vortex air and the surfaces of N_{10nv} . The smallest vertical gradient is observed for
653 ESSenCe (December) and the largest for RECONCILE (dominated by the March observations up

654 to 470 K). The corresponding values for EUPLEX (dominated by the January data up to 500 K)
655 lie in between.

656 (b.) $N_{10\text{nv}}$ as a function of the N_2O mixing ratio (Figure 8b):

657 The agreement of the regression slopes between EUPLEX (i.e. -0.71 ± 0.05) and RECONCILE
658 (i.e. -0.68 ± 0.01) is remarkable. Only the absolute values of $N_{10\text{nv}}$ are shifted along the
659 ordinate by a factor of about 1.1. Note that in terms of the covered range of N_2O mixing ratio,
660 measurements of RECONCILE-B dominate the regression compared to the RECONCILE-A
661 period (cf. Figure 6a to Figure 6e together with Figure 7d through Figure 7f). Thus, the data
662 from the later mission period assume more weight in the regression calculation. Such a
663 weighting imbalance is less pronounced for the EUPLEX period, although the lowest N_2O
664 mixing ratios were detected predominantly during the earlier EUPLEX period. Finally, the
665 slopes and intercepts of the ESSenCe data regressions are quite different from those of the
666 other missions.

667 In summary, the observed correlations are qualitatively consistent with the expected
668 development of the $N_{10\text{nv}}\text{-N}_2\text{O}$ correlation inside the vortex over the course of the winter (as
669 outlined above). Starting from the original canonical mid-latitude correlation at the time the
670 vortex forms, inside the isolated vortex the mixing ratio $N_{10\text{nv}}$ will continuously increase on a
671 given N_2O surface: This is consistent with the observed increase of $N_{10\text{nv}}$ between ESSenCe
672 (December), EUPLEX (more weighted toward January data) and RECONCILE (dominated by
673 March data) and is most likely driven by diabatic dispersion, in accord with current
674 understanding of polar tracer transport (Plumb et al., 2002, and Plumb, 2007).

675 **6.3 Implications for PSC formation**

676 The import of refractory material into the vortex constitutes a strong source of particles for a
677 region where the relative isolation of the vortex supports chemical reactions. The non-volatile
678 particles carried from aloft are most likely incorporated by stratospheric sulfate aerosol or
679 covered with sulfuric acid and provide surfaces for condensable materials and heterogeneous
680 chemical reactions (Peter, 1997; Wegner et al., 2012). PSC formation is usually thought to occur
681 by heterogeneous nucleation on the homogeneously nucleated $\text{H}_2\text{SO}_4\text{-H}_2\text{O}$ -droplets of the
682 stratospheric background aerosol. It may be assumed that stratospheric cloud elements also, or
683 even preferably, form on pre-existing condensation surfaces (Hoyle et al., 2013; Engel et al.,
684 2013) as provided by refractory particles, eminently at times when stratospheric background
685 aerosol concentrations are low. In particular, this process may be relevant in the polar
686 stratosphere with a low degree of HNO_3 -supersaturation (Voigt et al., 2005), which is a
687 frequently occurring condition in the Arctic.

688 Based on our data, up to 75 % by number of the aerosol particles inside the vortex are, or
689 contain, refractory cores with a diameter larger than 10 nm. Their presence contributes to the
690 probability that PSC elements can form, either directly, if the refractory cores have uncoated or
691 partially coated surfaces, or indirectly, if the cores are fully incorporated in a droplet of
692 condensable material. A measure of the grade of coating of each refractory aerosol is not
693 obtainable with the COPAS technique. The ability of an uncoated or partially coated refractory
694 aerosol particle to act as a PSC condensation nucleus may strongly depend on the chemical
695 composition and surface property of the individual particle. Incorporated in a droplet, the ability
696 of acting as a PSC condensation nucleus should not differ from that of a pure, e.g., H_2SO_4 droplet
697 if the core is inert and insoluble. If, in contrast, parts of the refractory core are dissolved,
698 important chemical conversion or electric charges and polarity may influence the ability of such

699 a solution droplet to support PSC formation. In conclusion, the refractory particles support the
700 availability of condensation surfaces, and therefore the probability that stratospheric cloud
701 particles form only homogeneously is diminished. Of course, our measurements cannot exclude
702 that PSCs form via new particle formation at even higher altitudes than explored by our mission
703 flights. However, above an altitude of 27 km the ambient temperatures becomes too high
704 (> 195 K ambient temperature) and the vapor saturation too low for new particle formation of
705 PSC elements to occur.

706 **6.4 Estimates of the refractory aerosol mass contained in the vortex**

707 **6.4.1 Calculation steps**

708 In order to estimate the total amount of refractory submicron aerosol contained inside the Arctic
709 vortex the following steps were taken:

710 (1.) The vortex cross sectional areas (VCSAs) are calculated by means of the CLaMS model in
711 potential temperature bins of 10 K. For the Θ -range of 400 - 500 K the VCSAs are averaged over
712 the respective campaign duration (cf. Section 2, results in Table 3). The determined VCSAs
713 include the horizontally almost homogeneous parts of the vortex for which the selected
714 observations with values of ξ_{vi} higher than 0.75 are representative. Thus, air recently intruding
715 from mid-latitudes is not included.

716 (2.) Based on the regressions shown in Figure 8a, the mixing ratios N_{10nv} are parameterized
717 as a function of the potential temperature (Table 1).

718 (3.) The available stratospheric aerosol size distributions are parameterized as a sum of
719 lognormal distribution functions, where they are not already given in that form in literature.
720 From these lognormal distributions, applying the Hatch-Choate equations (Hinds, 1999), the
721 diameter of average volume and the total volume concentration are calculated. From the total
722 volume and total number concentrations the average volume per particle v_p is computed.

723 (3a) As a lowermost limit of this estimate the modelled size distribution of meteoritic
724 ablation material at 30 km altitude above the winter pole is taken (Bardeen et al., 2008 and
725 cf. Figure 1). For the mean volume per particle v_p this size distribution yields $3.1 \times 10^{-23} \text{ m}^3$.
726 The uncertainty with respect to the resulting mean aerosol mass value is mainly given by the
727 range of material densities (cf. Step 7 in this list).

728 (3b) As the uppermost limit of this estimate the parameterized model size
729 distributions of stratospheric aerosol from three different studies (Jaenicke, 1980; Wang et
730 al., 1989 and Deshler, 2008) are considered. The volume per particle is given as a volume
731 range (cf. Table 2) resulting from the range of underlying size distributions (Figure 1). We
732 consider the uncertainty as the maximum range of average volumes per particle derived
733 from these size distributions available in literature.

734 (4.) The total particle volume per air mass (in $\text{m}^3 \text{ kg}^{-1}$) is calculated from N_{10nv} and the
735 average volume per particle from Step 3 as a function of the potential temperature.

736 (5.) The Θ - p -relationship is parameterized based on measurements for the respective Arctic
737 campaign (Table 2). For each campaign the uncertainty is considered as the maximum range of
738 all measured relationships. The total air mass is then calculated from the VCSA values from
739 Step 1 and the pressure differences at chosen Θ -levels which have a distance of 10 K from each
740 other.

741 (6.) The total particle volume per Θ -level is calculated from the total air mass per Θ -level and
742 the particle volume ratio (in $\text{m}^3 \text{ kg}^{-1}$) for the corresponding level.

743 (7.) The total particle mass per Θ -level is calculated from the total particle volume and the
744 particle density. We consider the uncertainty of the particle density as the range between unit
745 density ($\rho_p = 1000 \text{ kg m}^{-3}$) and the density of solid meteoritic material. To account for chemical
746 conversion of meteoritic material, e.g. into salts, a material density ρ_p of 3000 kg m^{-3} is chosen as
747 the uppermost limit (cf. Table 2). This relatively high value of ρ_p is justified by the maximum
748 material density reached by iron sulfate hydrates, a possible remnant of dissolved meteoritic
749 material in H_2SO_4 . For the estimate $\rho_p = 2000 \text{ kg m}^{-3}$ is chosen as the mean value of the material
750 densities range. The total particle mass is obtained as the sum of all Θ -levels between 400 K and
751 500 K (Table 3) for which particle data were available.

752 Of course there are considerable uncertainties inherent in such estimates:

753 (a.) About a factor of 5 in uncertainty is implied in v_p from the range of size distributions. The
754 therein included, but most important uncertainty arises from the unknown true size distribution
755 of refractory particles with diameters between 10 nm - 1 μm . COPAS detects the particles of this
756 size range, but does not size them.

757 (b.) Further uncertainties of a factor of 1.2 come from the $\Theta - p$ - relationship, and an additional
758 uncertainty factor of 1.7 results from the range of particle material densities ρ_p .

759 (c.) Also, it has to be considered that substantial amounts of refractory aerosol descending in the
760 vortex are not accounted for in our approach. Examples are those particles in the vortex edge
761 region or within and below the vortex bottom transition zone, as well as particles which
762 isentropically escaped from the vortex to mid-latitudes prior to the observation period.

763 (d.) Due to the COPAS activation limit and the inlet transmission, particles of diameters smaller
764 than 10 nm and larger than about 1 μm are disregarded (Weigel et al., 2009).

765 (e.) The model estimates of the VCSAs also involve uncertainties of at the most 50 %.

766 **6.4.2 Estimate results**

767 In Table 3 and Table 4 the results of our estimates are provided in terms of the altitude resolved
768 mass of refractory aerosol as a function of the potential temperature. The values for the
769 uppermost estimate are shown in Table 3 whilst the lowermost estimates are given in Table 4.
770 In the following mass values are provided with a superscript index (#) for a better traceability of
771 the data's origin.

772 The applied pressure altitudes for the Θ -levels indicate the various meteorological vortex
773 conditions of the different campaigns. The resulting uppermost estimate (Table 3) amounts to a
774 mass of approximately $45.6 \times 10^6 \text{ kg}$ ⁽¹⁾ in Table 3) of refractory aerosol in the vortex column
775 between 85 hPa and 49 hPa for EUPLEX. The ESSenCe case with estimated $21.3 \times 10^6 \text{ kg}$ ⁽²⁾ in
776 Table 3) of refractory particulate matter between 101 hPa and 56 hPa may provide a reference
777 for the conditions when the vortex air is not yet influenced by major particle import from above
778 during the current winter. The mean particle volume from the MSP size distribution (Bardeen et
779 al., 2008) ranges at three orders of magnitude below corresponding values of the upper limit.
780 Thus, the lowermost estimate generally yields a refractory aerosol mass which is a factor of
781 1000 less (Table 4) than obtained from the upper limit within the vortex. The largest estimated
782 mass in the probed vortex column comes from the RECONCILE measurements ⁽³⁾ in Table 3)
783 which are dominated by data from March, i.e. the late Arctic winter.

784 Within a pressure range of 100 - 67 hPa the derived refractory aerosol masses from RECONCILE
785 and ESSenCe are directly comparable. Presuming that the vortices undergo similar
786 developments throughout the different winters (which in reality is not the case) the mass
787 difference constitutes an enhancement of refractory aerosol by a factor of 4.5 during three

788 months from December through March (ratio of ⁽⁴⁾ and ⁽⁵⁾ in Table 3 and of ⁽⁶⁾ and ⁽⁷⁾ in Table 4).
789 With the mean upper limit of this estimate the differential enhancement ranges at 37.5×10^6 kg
790 (difference between ⁽⁴⁾ and ⁽⁵⁾ in Table 3) and correspondingly for the lowermost limit
791 23.3×10^3 kg (difference between ⁽⁶⁾ and ⁽⁷⁾ in Table 4) of refractory aerosol material within the
792 vortex over the course of a winter.

793 Indeed, our observations made during ESSenCE most likely represent the conditions within the
794 lower vortex region prior to the arrival of additional refractory particles from above. Assuming
795 the simulation of Plumb et al. (2002) to be realistic, and since the air mass is twice as large in the
796 column 67 to 1 hPa as in the observed column 100 to 67 hPa, we estimate that at the end of the
797 Arctic winter about 10 – 30 % of the mesospheric air mass contributing to the entire vortex
798 volume is to be found in the measurement region below 470 K (see Figure 6 in Plumb et al.,
799 2002). We assume further that the increase by a factor of 4.5 in the observed particle mass
800 between 100 hPa and 67 hPa from mid-December to late winter can be attributed to the
801 downward transport of refractory particles. The outflow of these particles at the vortex bottom
802 may be negligible compared to the import from aloft. Hence, applying division by 0.3 and 0.1 to
803 the mass enhancement obtained within the probed vortex regime, the particle import from the
804 mesosphere is inferred, with an uppermost (lowermost) limit over the entire vortex of about
805 $^{(8)}125 - 375 \times 10^6$ kg ($77 - 230 \times 10^3$ kg) for the RECONCILE winter 2009/2010.

806 **6.4.3 Constraining the size distribution of the vortex refractory aerosol**

807 The expected global influx of meteoritic material is about 110×10^3 kg per day (Love and
808 Brownlee, 1993). Thus, per year up to $^{(9)}40 \times 10^6$ kg of meteoritic material may be deposited in
809 the mesosphere. Parts of the recently deposited aerosol material may remain in the mesosphere
810 for several years (Dhomse et al., 2013). Nevertheless, a certain fraction of the recently deposited
811 material may descend out of the mesosphere due to the vortex-induced subsidence during the
812 next polar winter. When the vortex disintegrates in early spring the particles are horizontally
813 spread towards mid-latitudes over the entire vertical extension of the former vortex column.
814 Over the following seasons, until a new vortex can form, a certain fraction of particles may
815 remain in the region above the pole. This fraction is available for incorporation into the newly
816 forming vortex leading to further descent of particles. Finally, these particles reach the
817 lowermost part of the vortex at $\Theta < 500$ K ahead of the newly incoming mesospheric air in early
818 winter. However, for a balanced mass budget, the amount of material exiting the mesosphere
819 towards the stratosphere should be in the range of the mesospheric input. Otherwise the
820 meteoritic ablation material would accumulate in the mesosphere.

821 Thus, assuming a steady state situation and symmetry between the two hemispheres, each polar
822 vortex would remove half of the amount of the yearly influx (⁽⁹⁾, cf. above) over the course of a
823 winter, i.e. 20×10^6 kg. Consequently, the refractory aerosol mass calculated from the size
824 distribution of MSPs at 30 km above the winter pole (Bardeen et al., 2008) yields values, i.e.
825 23.3×10^3 kg (difference between ⁽⁶⁾ and ⁽⁷⁾ in Table 4), two orders of magnitude below the
826 expected mass influx. One could speculate that the vertical removal of meteoritic material occurs
827 more efficiently at lower latitudes than due to the polar vortices, but this would contradict the
828 findings that, at the end of a polar winter, most of the mesospheric content has been ingested by
829 the vortex (Plumb et al., 2002). Therefore, the meteoritic ablation material is most likely drained
830 to a large extent out of the mesosphere via the winter vortex. Consequently, the lowermost limit
831 of our estimate seems to significantly underestimate the mass of refractory aerosol within the
832 vortex. The size distribution of Bardeen et al. (2008), if adjusted for the size range of $d_p > 10$ nm

833 to be in accordance with N_{10nv} , results in an in-vortex mass of refractory aerosol that is much
834 smaller than could be expected.

835 The size distributions that our estimates are based on only provide certain limits of such
836 calculations. The true refractory aerosol size distribution, which is currently unknown, may be
837 located somewhere in between the minimum of the stratospheric background aerosol (Jaenicke,
838 1980; Wang et al., 1989; Deshler, 2008) and the numerically derived size distribution of MSPs
839 (Bardeen et al., 2008). Nevertheless, the size distribution of the non-volatile remnants that
840 remain, after the volatile compounds are evaporated, may not significantly differ from a typical
841 size distribution of an aged, processed aerosol. Thus, it seems conceivable that the true
842 refractory aerosol size distribution is very similar in shape to the size distribution of the
843 stratospheric background aerosol, but this true refractory aerosol size distribution may peak at
844 a certain smaller particle size. To sufficiently drain the expected meteoritic influx the true size
845 distribution should result in an integrated refractory aerosol mass inside the entire vortex that
846 is of the magnitude of the half-year influx, i.e. 20×10^6 kg. Our estimate nearly approaches such
847 a value with a tenth of the upper estimate's mean, i.e. $11.2 - 37.5 \times 10^6$ kg (tenth of ⁽⁸⁾, cf. end of
848 Sections 6.4.2). This value still ranges at the lowermost extreme within this upper limit's
849 uncertainty (⁽¹⁰⁾ and ⁽¹¹⁾ in Table 3). However, the amount of the daily influx of meteoritic
850 material is a matter of debate and could be a tenth (Plane, 2012) of what is specified by other
851 references (Love and Brownlee, 1993; von Zahn, 2005). The true size distribution of refractory
852 aerosol within the vortex will most likely peak at sizes smaller than the stratospheric
853 background aerosol. However, as a hypothesis, the distribution may peak closer to our
854 estimate's upper limit rather than being strongly shifted towards the estimate's lowermost limit.

855 There is the need to account for the probability that parts of the refractory aerosol in the Arctic
856 vortex may originate from sources other than the meteoritic ablation in the mesosphere. These
857 particles, e.g. from air and space traffic, sub-Pinatubo volcanism, biomass burning, etc., may
858 contribute to the size distribution of refractory aerosol in the vortex. The negative correlation
859 with N_2O within the vortex indicates however that these refractory aerosols previously resided
860 at high altitudes. The Brewer-Dobson-circulation serves as the most important pathway leading
861 the stratospheric material at high altitudes towards the pole, requiring these particles to survive
862 a long-range transport. This condition is best fulfilled when the size of these refractory particle
863 ranges within the accumulation mode ($0.1 < d_p < 1 \mu m$) which has longest atmospheric life times.
864 The hypothesized contribution of submicron particles from other sources would be strongly
865 supported if such particle species having an origin other than the meteoritic ablation were
866 identified within the vortex.

867 In conclusion, estimations such as ours bear many uncertainties, but this clearly shows that
868 comprehensive in-situ investigations are necessary with respect to the different sources and
869 transport mechanisms of refractory aerosol in the stratosphere to eliminate the current
870 ambiguities. Also such in-situ measurements of refractory aerosols at high altitudes may be used
871 for refining the boundary conditions of numerical models simulating the vortex dynamics.

872 **7 Summary and Conclusions**

873 Inside the Arctic vortex up to 8 of 11 particles with diameters larger than 10 nm and smaller
874 than about $1 \mu m$ were observed to consist of non-volatile material. During three Arctic winter
875 seasons of the years 2003, 2010 and 2011 this observation was repeatedly made in qualitative
876 agreement. This agreement leads to the conclusion that the import of refractory aerosol material
877 in the Arctic polar winter is a regular feature. We surmise that earlier observations of increased

878 aerosol number concentration inside the Arctic vortex at about 20 km altitude (Wilson et al.,
879 1990) and above 20 km (Hofmann et al., 1990) also comprise refractory aerosol and that new
880 particle formation by homogeneous nucleation at the considered high altitudes plays a less
881 crucial role than previously thought.

882 The quantity of refractory aerosols inside the vortex is connected to the transport history of air
883 masses entering the vortex upper boundary from aloft which includes air that could originate
884 from as high as the mesosphere. Particle mixing ratios (up to 150 of non-volatile particles per
885 milligram air) and the fraction of non-volatile particles (up to 75 %) are highest, where the air
886 mass content of nitrous oxide (N_2O) is lowest (here down to 70 nmol mol⁻¹). The largest amounts
887 of refractory aerosol inside the vortex appear in late winter (March), while in early winter
888 (December) the bulk import from the upper stratosphere or mesosphere has apparently not yet
889 reached the lower vortex observation region. In general the observed evolution of refractory
890 particles and their correlation with the conserved tracer N_2O in the Arctic vortex are in accord
891 with current understanding of tracer transport and with the theory of tracer-tracer correlations
892 (Plumb et al., 2002 and Plumb, 2007). Based on this evolution of vertical profiles and
893 correlations with N_2O we suggest here that, apart from mean subsidence, transport of refractory
894 aerosol to the lower vortex may be significantly driven by diabatic dispersion resulting from
895 differential subsidence and mixing within the vortex. As shown here, until late March the
896 refractory aerosol from high altitudes reaches down to the vortex bottom at about 400 K, which
897 could not be explained to result only from the slow mean subsidence in the lower vortex. At the
898 end of March the downward motion inside the Arctic vortex diminishes. Later the vortex
899 dissolves releasing the ingested material for mixing towards mid-latitudes. The vortex can thus
900 be understood as a temporary stratospheric reservoir of refractory aerosol material imported
901 from aloft.

902 The abundance of refractory aerosol in the winter vortex is significantly driven by (a.) the source
903 strength (ablation of penetrating meteorites, volcanic activity, or other sources) for the aerosol
904 material, (b.) Rossby and gravity wave forcing driving the meridional circulations in the
905 mesosphere and stratosphere, including the polar winter descent of air from high altitudes and
906 (c.) the vortex stability, as mid-winter stratospheric warmings and vortex break-up facilitate air
907 mass exchange across the vortex boundary resulting in dilution of the vortex with air from lower
908 latitudes.

909 It can be assumed that over the course of a winter season the import of refractory aerosol due to
910 the winter vortex subsidence and diabatic dispersion also occurs in the Antarctic. Recent studies
911 (Campbell and Deshler, 2014) indicate that occasionally new particle formation contributes to
912 the Antarctic aerosol loading at altitudes of 21-24 km. Nevertheless, also in the Antarctic, but
913 above 24 km, fractions of up to 80 % of non-volatile particles were observed.

914 From our measurements we have estimated the total refractory aerosol mass in the lowermost
915 vortex and further the aerosol mass imported from aloft into the pressure interval 100 – 67 hPa
916 between early (ESSenCe) and late winter (RECONCILE). This estimate yields an enhancement of
917 the refractory aerosol mass by a factor of 4.5 at the lowermost vortex (100 – 67 hPa) toward the
918 end of an Arctic winter. These estimates are further extrapolated to an estimate of the integrated
919 refractory aerosol mass import into the entire Arctic winter vortex, which is finally evaluated by
920 comparison with the assumed influx of meteoritic aerosol material. Of course, large
921 uncertainties are inherent in this approach. The largest ambiguity arises from the unknown size
922 distribution of refractory aerosol within the Arctic vortex. However, the value for the daily influx

923 of meteoritic material is still a matter of discussion, and it is still possible that non-meteoritic
924 sources contribute to the vortex refractory aerosol composition. Nonetheless, within the given
925 uncertainties our estimate of the integrated refractory aerosol mass reveals that the import into
926 the Arctic winter vortex could in principle balance the assumed meteoritic mass influx into the
927 mesosphere.

928 Consequently, the remaining unresolved issues are connected with the chemical composition,
929 the morphology, and physical nature of the refractory particles entering the polar vortex for
930 unambiguously specifying their origin. The amount and role of anthropogenic components from
931 space debris, rocket launches and exhaust of high flying aircraft is not well enough quantified.
932 Even contributions of soil materials continuously released by sub-Pinatubo volcanism (e.g.
933 Souffriere Hills, Nabro, etc.) and other ground sources, such as biomass burning, possibly need
934 to be considered. Knowledge of the aerosol properties is also essential for conclusions
935 concerning the particle sources as well as their role and effectiveness in PSC and, ultimately, in
936 cirrus cloud formation. Besides the need for more in-situ measurements at high altitudes we
937 would like to emphasize the importance of laboratory experiments on heterogeneous nucleation
938 of PSCs (particularly for NAT) on the observed refractory materials including particles coated
939 with H₂SO₄, HNO₃, H₂O, and possibly other condensable materials.

940 **Acknowledgements**

941 The contributions from the technical staff at the workshops of the MPI for Chemistry and the
942 Institute for Physics of the Atmosphere (Mainz University), as well as the Myasishchev Design
943 Bureau (MDB) were crucial and essential. In particular we acknowledge support of T. Böttger, M.
944 Flanz and W. Schneider. We very much thank the MDB crew and the M55-*Geophysica* pilots.
945 Thanks to R. E. Jubb for proof-reading the manuscript. ESSenCe was in parts supported by the
946 German Research Foundation (DFG) under contract HALO-SPP 1294/GR 3786. Some of our
947 research leading to the presented results received funding from the European Research Council
948 under the European Union's Seventh Framework Program (FP/2007-2013)/ERC Grant
949 Agreement No. 321040 (EXCATRO). RECONCILE was supported by ESA, BMBF, and the EU
950 (contract RECONCILE-226365-FP7-ENV-2008-1). Further financial support was provided by
951 internal sources of the Johannes-Gutenberg University and the Max-Planck-Institute for
952 Chemistry in Mainz, as well as the Karlsruhe Institute for Technology and Forschungszentrum
953 Jülich GmbH (both for ESSenCe). We dedicate this publication to our colleague and friend, Dr.
954 Cornelius Schiller, who was involved in EUPLEX and RECONCILE, and who passed away so
955 untimely on March 3, 2012.

956 **References**

957 Bardeen, C. G., Toon, O. B., Jensen, E. J., Marsh, D. R., and Harvey, V. L.: Numerical simulations of
958 the three-dimensional distribution of meteoric dust in the mesosphere and upper stratosphere,
959 *Journal of Geophysical Research: Atmospheres*, 113, D17202, 10.1029/2007jd009515, 2008.

960 Biermann, U. M., Presper, T., Koop, T., Mossinger, J., Crutzen, P. J., and Peter, T.: The unsuitability
961 of meteoritic and other nuclei for polar stratospheric cloud freezing, *Geophys Res Lett*, 23, 1693-
962 1696, Doi 10.1029/96gl01577, 1996.

963 Borrmann, S., Dye, J. E., Baumgardner, D., Proffitt, M. H., Margitan, J. J., Wilson, J. C., Jonsson, H. H.,
964 Brock, C. A., Loewenstein, M., Podolske, J. R., and Ferry, G. V.: Aerosols as Dynamical Tracers in

- 965 the Lower Stratosphere - Ozone Versus Aerosol Correlation after the Mount-Pinatubo Eruption, *J*
966 *Geophys Res-Atmos*, 100, 11147-11156, Doi 10.1029/95jd00016, 1995.
- 967 Borrmann, S., Thomas, A., Rudakov, V., Yushkov, V., Lepuchov, B., Deshler, T., Vinnichenko, N.,
968 Khattatov, V., and Stefanutti, L.: Stratospheric aerosol measurements in the Arctic winter of
969 1996/1997 with the M-55 Geophysika high-altitude research aircraft, *Tellus B*, 52, 1088-1103,
970 DOI 10.1034/j.1600-0889.2000.00100.x, 2000.
- 971 Borrmann, S., Kunkel, D., Weigel, R., Minikin, A., Deshler, T., Wilson, J. C., Curtius, J., Volk, C. M.,
972 Homan, C. D., Ulanovsky, A., Ravegnani, F., Viciani, S., Shur, G. N., Belyaev, G. V., Law, K. S., and
973 Cairo, F.: Aerosols in the tropical and subtropical UT/LS: in-situ measurements of submicron
974 particle abundance and volatility, *Atmos Chem Phys*, 10, 5573-5592, DOI 10.5194/acp-10-5573-
975 2010, 2010.
- 976 Brock, C. A., Hamill, P., Wilson, J. C., Jonsson, H. H., and Chan, K. R.: Particle Formation in the
977 Upper Tropical Troposphere: A Source of Nuclei for the Stratospheric Aerosol, *Science*, 270,
978 1650-1653, 10.2307/2887916, 1995.
- 979 Campbell, P., and Deshler, T.: Condensation nuclei measurements in the midlatitude (1982–
980 2012) and Antarctic (1986–2010) stratosphere between 20 and 35 km, *Journal of Geophysical*
981 *Research: Atmospheres*, 119, 2013JD019710, 10.1002/2013jd019710, 2014.
- 982 Curtius, J., Weigel, R., Vössing, H. J., Wernli, H., Werner, A., Volk, C. M., Konopka, P., Krebsbach, M.,
983 Schiller, C., Roiger, A., Schlager, H., Dreiling, V., and Borrmann, S.: Observations of meteoric
984 material and implications for aerosol nucleation in the winter Arctic lower stratosphere derived
985 from in situ particle measurements, *Atmos Chem Phys*, 5, 3053-3069, 2005.
- 986 Cziczo, D. J., Thomson, D. S., and Murphy, D. M.: Ablation, flux, and atmospheric implications of
987 meteors inferred from stratospheric aerosol, *Science*, 291, 1772-1775, 2001.
- 988 Deshler, T.: A review of global stratospheric aerosol: Measurements, importance, life cycle, and
989 local stratospheric aerosol, *Atmospheric Research*, 90, 223-232, DOI
990 10.1016/j.atmosres.2008.03.016, 2008.
- 991 Dhomse, S. S., Saunders, R. W., Tian, W., Chipperfield, M. P., and Plane, J. M. C.: Plutonium-238
992 observations as a test of modeled transport and surface deposition of meteoric smoke particles,
993 *Geophys Res Lett*, 40, 4454-4458, 10.1002/grl.50840, 2013.
- 994 Dörnbrack, A., Pitts, M. C., Poole, L. R., Orsolini, Y. J., Nishii, K., and Nakamura, H.: The 2009–2010
995 Arctic stratospheric winter – general evolution, mountain waves and predictability of an
996 operational weather forecast model, *Atmos. Chem. Phys.*, 12, 3659-3675, 10.5194/acp-12-3659-
997 2012, 2012.
- 998 Engel, A., Möbius, T., Haase, H. P., Bönisch, H., Wetter, T., Schmidt, U., Levin, I., Reddman, T.,
999 Oelhaf, H., Wetzol, G., Grunow, K., Huret, N., and Pirre, M.: Observation of mesospheric air inside
1000 the arctic stratospheric polar vortex in early 2003, *Atmos. Chem. Phys.*, 6, 267-282,
1001 10.5194/acp-6-267-2006, 2006.
- 1002 Engel, I., Luo, B. P., Pitts, M. C., Poole, L. R., Hoyle, C. R., Grooss, J. U., Dornbrack, A., and Peter, T.:
1003 Heterogeneous formation of polar stratospheric clouds - Part 2: Nucleation of ice on synoptic
1004 scales, *Atmos Chem Phys*, 13, 10769-10785, DOI 10.5194/acp-13-10769-2013, 2013.
- 1005 Fahey, D. W., Kelly, K. K., Kawa, S. R., Tuck, A. F., Loewenstein, M., Chan, K. R., and Heidt, L. E.:
1006 Observations of Denitrification and Dehydration in the Winter Polar Stratospheres, *Nature*, 344,
1007 321-324, Doi 10.1038/344321a0, 1990.

- 1008 Fisher, M., O'Neill, A., and Sutton, R.: Rapid descent of mesospheric air into the stratospheric
1009 polar vortex, *Geophys Res Lett*, 20, 1267-1270, 10.1029/93gl01104, 1993.
- 1010 Frey, W., Borrmann, S., Kunkel, D., Weigel, R., de Reus, M., Schlager, H., Roiger, A., Voigt, C., Hoor,
1011 P., Curtius, J., Kramer, M., Schiller, C., Volk, C. M., Homan, C. D., Fierli, F., Di Donfrancesco, G.,
1012 Ulanovsky, A., Ravegnani, F., Sitnikov, N. M., Viciani, S., D'Amato, F., Shur, G. N., Belyaev, G. V.,
1013 Law, K. S., and Cairo, F.: In situ measurements of tropical cloud properties in the West African
1014 Monsoon: upper tropospheric ice clouds, Mesoscale Convective System outflow, and subvisual
1015 cirrus, *Atmos Chem Phys*, 11, 5569-5590, DOI 10.5194/acp-11-5569-2011, 2011.
- 1016 Funke, B., García-Comas, M., López-Puertas, M., Glatthor, N., Stiller, G. P., von Clarmann, T.,
1017 Semeniuk, K., and McConnell, J. C.: Enhancement of N₂O during the October–November 2003
1018 solar proton events, *Atmos. Chem. Phys.*, 8, 3805-3815, 10.5194/acp-8-3805-2008, 2008.
- 1019 Gabrielli, P., Barbante, C., Plane, J. M. C., Varga, A., Hong, S., Cozzi, G., Gaspari, V., Planchon, F. A.
1020 M., Cairns, W., Ferrari, C., Crutzen, P., Cescon, P., and Boutron, C. F.: Meteoric smoke fallout over
1021 the Holocene epoch revealed by iridium and platinum in Greenland ice, *Nature*, 432, 1011-1014,
1022 Doi 10.1038/Nature03137, 2004.
- 1023 Greenblatt, J. B., Jost, H.-J., Loewenstein, M., Podolske, J. R., Hurst, D. F., Elkins, J. W., Schauffler, S.
1024 M., Atlas, E. L., Herman, R. L., Webster, C. R., Bui, T. P., Moore, F. L., Ray, E. A., Oltmans, S., Vömel,
1025 H., Blavier, J.-F., Sen, B., Stachnik, R. A., Toon, G. C., Engel, A., Müller, M., Schmidt, U., Bremer, H.,
1026 Pierce, R. B., Sinnhuber, B.-M., Chipperfield, M., and Lefèvre, F.: Tracer-based determination of
1027 vortex descent in the 1999/2000 Arctic winter, *Journal of Geophysical Research: Atmospheres*,
1028 107, 8279, 10.1029/2001jd000937, 2002a.
- 1029 Greenblatt, J. B., Jost, H.-J., Loewenstein, M., Podolske, J. R., Bui, T. P., Hurst, D. F., Elkins, J. W.,
1030 Herman, R. L., Webster, C. R., Schauffler, S. M., Atlas, E. L., Newman, P. A., Lait, L. R., Müller, M.,
1031 Engel, A., and Schmidt, U.: Defining the polar vortex edge from an N₂O:potential temperature
1032 correlation, *Journal of Geophysical Research: Atmospheres*, 107, 8268, 10.1029/2001jd000575,
1033 2002b.
- 1034 Grooß, J. U., Engel, I., Borrmann, S., Frey, W., Günther, G., Hoyle, C. R., Kivi, R., Luo, B. P., Mollenker,
1035 S., Peter, T., Pitts, M. C., Schlager, H., Stiller, G., Vömel, H., Walker, K. A., and Müller, R.: Nitric acid
1036 trihydrate nucleation and denitrification in the Arctic stratosphere, *Atmos. Chem. Phys.*, 14,
1037 1055-1073, 10.5194/acp-14-1055-2014, 2014.
- 1038 Günther, G., Müller, R., von Hobe, M., Stroh, F., Konopka, P., and Volk, C. M.: Quantification of
1039 transport across the boundary of the lower stratospheric vortex during Arctic winter
1040 2002/2003, *Atmos. Chem. Phys.*, 8, 3655-3670, 10.5194/acp-8-3655-2008, 2008.
- 1041 Haynes, P., and Shuckburgh, E.: Effective diffusivity as a diagnostic of atmospheric transport: 1.
1042 Stratosphere, *Journal of Geophysical Research: Atmospheres*, 105, 22777-22794,
1043 10.1029/2000jd900093, 2000.
- 1044 Hinds, W. C.: *Aerosol Technology: Properties, Behavior, and Measurement of airborne Particles*
1045 (2nd edition), 1999.
- 1046 Hofmann, D. J., Deshler, T., Arnold, F., and Schlager, H.: Balloon Observations of Nitric-Acid
1047 Aerosol Formation in the Arctic Stratosphere .2. Aerosol, *Geophys Res Lett*, 17, 1279-1282, Doi
1048 10.1029/Gl017i009p01279, 1990.
- 1049 Holton, J. R., Haynes, P. H., McIntyre, M. E., Douglass, A. R., Rood, R. B., and Pfister, L.:
1050 Stratosphere-troposphere exchange, *Rev Geophys*, 33, 403-439, 1995.

- 1051 Homan, C. D., Volk, C. M., Kuhn, A. C., Werner, A., Baehr, J., Viciani, S., Ulanovski, A., and
 1052 Ravegnani, F.: Tracer measurements in the tropical tropopause layer during the AMMA/SCOUT-
 1053 O3 aircraft campaign, *Atmos Chem Phys*, 10, 3615-3627, 2010.
- 1054 Hösen, E., Volk, C. M., Grooß, J.-U., Günther, G., and Werner, A.: The vortex index: An empirical
 1055 origin of air tracer based on long-lived tracer measurements, submitted to *ACPD*, 2014.
- 1056 Hoyle, C. R., Engel, I., Luo, B. P., Pitts, M. C., Poole, L. R., Grooss, J. U., and Peter, T.: Heterogeneous
 1057 formation of polar stratospheric clouds - Part 1: Nucleation of nitric acid trihydrate (NAT),
 1058 *Atmos Chem Phys*, 13, 9577-9595, DOI 10.5194/acp-13-9577-2013, 2013.
- 1059 Hunten, D. M., Turco, R. P., and Toon, O. B.: Smoke and Dust Particles of Meteoric Origin in the
 1060 Mesosphere and Stratosphere, *Journal of the Atmospheric Sciences*, 37, 1342-1357, 1980.
- 1061 Jaenicke, R.: Atmospheric Aerosols and Global Climate, *J Aerosol Sci*, 11, 577-588, Doi
 1062 10.1016/0021-8502(80)90131-7, 1980.
- 1063 Jones, J., and Kaiser, T. R.: The effects of thermal radiation, conduction and meteoroid heat
 1064 capacity on meteoric ablation, *Mon Not R Astron Soc*, 133, 1966.
- 1065 Kalashnikova, O., Horányi, M., Thomas, G. E., and Toon, O. B.: Meteoric smoke production in the
 1066 atmosphere, *Geophys Res Lett*, 27, 3293-3296, 10.1029/1999gl011338, 2000.
- 1067 Kaufmann, M., Blank, J., Guggenmoser, T., Ungermann, J., Engel, A., Ern, M., Friedl-Vallon, F.,
 1068 Gerber, D., Grooss, J.-U., Günther, G., Höpfner, M., Kleinert, A., Latzko, T., Maucher, G., Neubert, T.,
 1069 Nordmeyer, H., Oelhaf, H., Olschewski, F., Orphal, J., Preusse, P., Schlager, H., Schneider, H.,
 1070 Schuettmeyer, D., Stroh, F., Suminska-Ebersoldt, O., Vogel, B., Volk, M., Wintel, J., Woiwode, W.,
 1071 and Riese, M.: Retrieval of three-dimensional small scale structures in upper tropospheric /
 1072 lower stratospheric composition as measured by GLORIA, submitted to *Atmos. Meas. Tech.*
 1073 *Discuss.*, 2014.
- 1074 Konopka, P., Günther, G., Müller, R., dos Santos, F. H. S., Schiller, C., Ravegnani, F., Ulanovsky, A.,
 1075 Schlager, H., Volk, C. M., Viciani, S., Pan, L. L., McKenna, D. S., and Riese, M.: Contribution of mixing
 1076 to upward transport across the tropical tropopause layer (TTL), *Atmos. Chem. Phys.*, 7, 3285-
 1077 3308, 10.5194/acp-7-3285-2007, 2007.
- 1078 Love, S. G., and Brownlee, D. E.: A Direct Measurement of the Terrestrial Mass Accretion Rate of
 1079 Cosmic Dust, *Science*, 262, 550-553, DOI 10.1126/science.262.5133.550, 1993.
- 1080 Mann, G. W., Davies, S., Carslaw, K. S., and Chipperfield, M. P.: Factors controlling Arctic
 1081 denitrification in cold winters of the 1990s, *Atmos Chem Phys*, 3, 403-416, 2003.
- 1082 McKenna, D. S., Grooß, J.-U., Günther, G., Konopka, P., Müller, R., Carver, G., and Sasano, Y.: A new
 1083 Chemical Lagrangian Model of the Stratosphere (CLaMS) 2. Formulation of chemistry scheme
 1084 and initialization, *Journal of Geophysical Research: Atmospheres*, 107, ACH 4-1-ACH 4-14,
 1085 10.1029/2000jd000113, 2002a.
- 1086 McKenna, D. S., Konopka, P., Grooß, J.-U., Günther, G., Müller, R., Spang, R., Offermann, D., and
 1087 Orsolini, Y.: A new Chemical Lagrangian Model of the Stratosphere (CLaMS) 1. Formulation of
 1088 advection and mixing, *Journal of Geophysical Research: Atmospheres*, 107, ACH 15-11-ACH 15-
 1089 15, 10.1029/2000jd000114, 2002b.
- 1090 Megner, L., Siskind, D. E., Rapp, M., and Gumbel, J.: Global and temporal distribution of meteoric
 1091 smoke: A two-dimensional simulation study, *Journal of Geophysical Research: Atmospheres*,
 1092 113, D03202, 10.1029/2007jd009054, 2008.

- 1093 Molleker, S., Borrmann, S., Schlager, H., Luo, B., Frey, W., Klingebiel, M., Weigel, R., Ebert, M.,
1094 Mitev, V., Matthey, R., Peter, T., Woiwode, W., Dörnbrack, A., Günther, G., Vogel, B., Grooß, J.-U.,
1095 Spelten, N., and Cairo, F.: Microphysical properties of synoptic scale polar stratospheric clouds:
1096 In-situ measurements of unexpectedly large HNO₃ containing particles in the Arctic vortex,
1097 submitted to ACPD, 2014.
- 1098 Murphy, D. M., Froyd, K. D., Schwarz, J. P., and Wilson, J. C.: Observations of the chemical
1099 composition of stratospheric aerosol particles, *Q J Roy Meteor Soc*, n/a-n/a, 10.1002/qj.2213,
1100 2013.
- 1101 Nash, E. R., Newman, P. A., Rosenfield, J. E., and Schoeberl, M. R.: An objective determination of
1102 the polar vortex using Ertel's potential vorticity, *Journal of Geophysical Research: Atmospheres*,
1103 101, 9471-9478, 10.1029/96jd00066, 1996.
- 1104 Peter, T.: Microphysics and heterogeneous chemistry of polar stratospheric clouds, *Annu Rev*
1105 *Phys Chem*, 48, 785-822, DOI 10.1146/annurev.physchem.48.1.785, 1997.
- 1106 Peter, T., and Grooß, J.-U.: Chapter 4 Polar Stratospheric Clouds and Sulfate Aerosol Particles:
1107 Microphysics, Denitrification and Heterogeneous Chemistry, in: *Stratospheric Ozone Depletion*
1108 *and Climate Change*, The Royal Society of Chemistry, 108-144, 2012.
- 1109 Peucker-Ehrenbrink, B.: Accretion of extraterrestrial matter during the last 80 million years and
1110 its effect on the marine osmium isotope record, *Geochimica et Cosmochimica Acta*, 60, 3187-
1111 3196, Doi 10.1016/0016-7037(96)00161-5, 1996.
- 1112 Plane, J. M. C.: A time-resolved model of the mesospheric Na layer: constraints on the meteor
1113 input function, *Atmos Chem Phys*, 4, 627-638, 2004.
- 1114 Plane, J. M. C.: Cosmic dust in the earth's atmosphere, *Chemical Society Reviews*, 41, 6507-6518,
1115 2012.
- 1116 Plumb, R. A., Heres, W., Neu, J. L., Mahowald, N. M., del Corral, J., Toon, G. C., Ray, E., Moore, F., and
1117 Andrews, A. E.: Global tracer modeling during SOLVE: High-latitude descent and mixing, *Journal*
1118 *of Geophysical Research: Atmospheres*, 107, 8309, 10.1029/2001jd001023, 2002.
- 1119 Plumb, R. A.: Tracer interrelationships in the stratosphere, *Rev Geophys*, 45, 2007.
- 1120 Prather, M. J., and Rodriguez, J. M.: Antarctic ozone: Meteoric control of HNO₃, *Geophys Res Lett*,
1121 15, 1-4, 10.1029/GL015i001p00001, 1988.
- 1122 Randall, C. E., Harvey, V. L., Singleton, C. S., Bernath, P. F., Boone, C. D., and Kozyra, J. U.: Enhanced
1123 NO_x in 2006 linked to strong upper stratospheric Arctic vortex, *Geophys Res Lett*, 33, L18811,
1124 10.1029/2006gl027160, 2006.
- 1125 Rapp, M., Strelnikova, I., and Gumbel, J.: Meteoric smoke particles: Evidence from rocket and
1126 radar techniques, *Adv Space Res*, 40, 809-817, DOI 10.1016/j.asr.2006.11.021, 2007.
- 1127 Rapp, M., and Strelnikova, I.: Measurements of meteor smoke particles during the ECOMA-2006
1128 campaign: 1. Particle detection by active photoionization, *Journal of Atmospheric and Solar-*
1129 *Terrestrial Physics*, 71, 477-485, DOI 10.1016/j.jastp.2008.06.002, 2009.
- 1130 Ray, E. A., Moore, F. L., Elkins, J. W., Hurst, D. F., Romashkin, P. A., Dutton, G. S., and Fahey, D. W.:
1131 Descent and mixing in the 1999-2000 northern polar vortex inferred from in situ tracer
1132 measurements, *Journal of Geophysical Research: Atmospheres*, 107, 8285,
1133 10.1029/2001jd000961, 2002.

- 1134 Saunders, R. W., Möhler, O., Schnaiter, M., Benz, S., Wagner, R., Saathoff, H., Connolly, P. J.,
 1135 Burgess, R., Murray, B. J., Gallagher, M., Wills, R., and Plane, J. M. C.: An aerosol chamber
 1136 investigation of the heterogeneous ice nucleating potential of refractory nanoparticles, *Atmos*
 1137 *Chem Phys*, 10, 1227-1247, DOI 10.5194/acp-10-1227-2010, 2010.
- 1138 Saunders, R. W., Dhomse, S., Tian, W. S., Chipperfield, M. P., and Plane, J. M. C.: Interactions of
 1139 meteoric smoke particles with sulphuric acid in the Earth's stratosphere, *Atmos Chem Phys*, 12,
 1140 4387-4398, DOI 10.5194/acp-12-4387-2012, 2012.
- 1141 Shur, G. N., Sitnikov, N. M., and Drynkov, A. V.: A mesoscale structure of meteorological fields in
 1142 the tropopause layer and in the lower stratosphere over the southern tropics (Brazil), *Russ.*
 1143 *Meteorol. Hydrol.*, 32, 487-494, 10.3103/s106837390708002x, 2007.
- 1144 Sokolov, L., and Lepuchov, B.: Protocol of interaction between Unit for Connection with Scientific
 1145 Equipment (UCSE) and on-board scientific equipment of Geophysica aircraft (Second edition),
 1146 Myasishchev Design Bureau (MDB), 1998.
- 1147 Solomon, S.: Stratospheric ozone depletion: A review of concepts and history, *Rev Geophys*, 37,
 1148 275-316, Doi 10.1029/1999rg900008, 1999.
- 1149 Spang, R., Stroh, F., von Hobe, M., Gerber, D., Moyna, B., Oldfield, M., Rea, S., Reburn, J., Siddans, R.,
 1150 Kerridge, B., Oelhaf, H., and Woiwode, W.: Data Acquisition Report of the PremierEX Scientific
 1151 Flights, Final Report for ESTEC, Contract No. 2670/09/NL/CT "PREMIER Experiment", 3139,
 1152 3151 https://earth.esa.int/documents/10174/87248/PremierEX_FinalReport_v2.pdf, 25 May,
 1153 2012.
- 1154 Stefanutti, L., Sokolov, L., Balestri, S., MacKenzie, A. R., and Khattatov, V.: The M-55 Geophysica as
 1155 a Platform for the Airborne Polar Experiment, *Journal of Atmospheric and Oceanic Technology*,
 1156 16, 1303-1312, 10.1175/1520-0426(1999)016<1303:tmgaap>2.0.co;2, 1999.
- 1157 Strelnikova, I., Rapp, M., Strelnikov, B., Baumgarten, G., Brattli, A., Svenes, K., Hoppe, U. P.,
 1158 Friedrich, M., Gumbel, J., and Williams, B. P.: Measurements of meteor smoke particles during the
 1159 ECOMA-2006 campaign: 2. Results, *Journal of Atmospheric and Solar-Terrestrial Physics*, 71,
 1160 486-496, DOI 10.1016/j.jastp.2008.07.011, 2009.
- 1161 Vogel, B., Konopka, P., Grooß, J. U., Müller, R., Funke, B., López-Puertas, M., Reddmann, T., Stiller,
 1162 G., von Clarmann, T., and Riese, M.: Model simulations of stratospheric ozone loss caused by
 1163 enhanced mesospheric NO_x during Arctic Winter 2003/2004, *Atmos. Chem. Phys.*, 8, 5279-5293,
 1164 10.5194/acp-8-5279-2008, 2008.
- 1165 Voigt, C., Schlager, H., Luo, B. P., Dornbrack, A. D., Roiger, A., Stock, P., Curtius, J., Vossing, H.,
 1166 Borrmann, S., Davies, S., Konopka, P., Schiller, C., Shur, G., and Peter, T.: Nitric Acid Trihydrate
 1167 (NAT) formation at low NAT supersaturation in Polar Stratospheric Clouds (PSCs), *Atmos Chem*
 1168 *Phys*, 5, 1371-1380, 2005.
- 1169 von Hobe, M., Bekki, S., Borrmann, S., Cairo, F., D'Amato, F., Di Donfrancesco, G., Dörnbrack, A.,
 1170 Ebersoldt, A., Ebert, M., Emde, C., Engel, I., Ern, M., Frey, W., Genco, S., Griessbach, S., Grooß, J. U.,
 1171 Gulde, T., Günther, G., Hösen, E., Hoffmann, L., Homonnai, V., Hoyle, C. R., Isaksen, I. S. A., Jackson,
 1172 D. R., Jánosi, I. M., Jones, R. L., Kandler, K., Kalicinsky, C., Keil, A., Khaykin, S. M., Khosrawi, F., Kivi,
 1173 R., Kuttippurath, J., Laube, J. C., Lefèvre, F., Lehmann, R., Ludmann, S., Luo, B. P., Marchand, M.,
 1174 Meyer, J., Mitev, V., Molleker, S., Müller, R., Oelhaf, H., Olschewski, F., Orsolini, Y., Peter, T.,
 1175 Pfeilsticker, K., Piesch, C., Pitts, M. C., Poole, L. R., Pope, F. D., Ravegnani, F., Rex, M., Riese, M.,
 1176 Röckmann, T., Rognerud, B., Roiger, A., Rolf, C., Santee, M. L., Scheibe, M., Schiller, C., Schlager, H.,
 1177 Siciliani de Cumis, M., Sitnikov, N., Søvde, O. A., Spang, R., Spelten, N., Stordal, F., Sumińska-
 1178 Ebersoldt, O., Ulanovski, A., Ungermann, J., Viciani, S., Volk, C. M., vom Scheidt, M., von der

1179 Gathen, P., Walker, K., Wegner, T., Weigel, R., Weinbruch, S., Wetzel, G., Wienhold, F. G.,
1180 Wohltmann, I., Woiwode, W., Young, I. A. K., Yushkov, V., Zobrist, B., and Stroh, F.: Reconciliation
1181 of essential process parameters for an enhanced predictability of Arctic stratospheric ozone loss
1182 and its climate interactions (RECONCILE): activities and results, *Atmos. Chem. Phys.*, 13, 9233-
1183 9268, 10.5194/acp-13-9233-2013, 2013.

1184 von Zahn, U.: The total mass flux of meteoroids into the Earth's upper atmosphere, 17th ESA
1185 Symposium on European Rocket and Balloon Programmes and Related Research, 30 May - 2
1186 June 2005, Sandefjord, Norway. Ed.: Barbara Warmbein. ESA SP-590, Noordwijk: ESA
1187 Publications Division, ISBN 92-9092-901-4, p. 33 - 39, 2005.

1188 Waibel, A. E., Peter, T., Carslaw, K. S., Oelhaf, H., Wetzel, G., Crutzen, P. J., Poschl, U., Tsias, A.,
1189 Reimer, E., and Fischer, H.: Arctic ozone loss due to denitrification, *Science*, 283, 2064-2069, DOI
1190 10.1126/science.283.5410.2064, 1999.

1191 Wang, P. H., McCormick, M. P., Swissler, T. J., Osborn, M. T., Fuller, W. H., and Yue, G. K.: Inference
1192 of Stratospheric Aerosol Composition and Size Distribution from Sage-II Satellite Measurements,
1193 *J Geophys Res-Atmos*, 94, 8435-8446, Doi 10.1029/Jd094id06p08435, 1989.

1194 Wegner, T., Grooss, J. U., von Hobe, M., Stroh, F., Suminska-Ebersoldt, O., Volk, C. M., Hosen, E.,
1195 Mitev, V., Shur, G., and Muller, R.: Heterogeneous chlorine activation on stratospheric aerosols
1196 and clouds in the Arctic polar vortex, *Atmos Chem Phys*, 12, 11095-11106, DOI 10.5194/acp-12-
1197 11095-2012, 2012.

1198 Weigel, R., Hermann, M., Curtius, J., Voigt, C., Walter, S., Bottger, T., Lepukhov, B., Belyaev, G., and
1199 Borrmann, S.: Experimental characterization of the CONDensation PARTICle counting System for
1200 high altitude aircraft-borne application, *Atmos Meas Tech*, 2, 243-258, 2009.

1201 Weigel, R., Borrmann, S., Kazil, J., Minikin, A., Stohl, A., Wilson, J. C., Reeves, J. M., Kunkel, D., de
1202 Reus, M., Frey, W., Lovejoy, E. R., Volk, C. M., Viciani, S., D'Amato, F., Schiller, C., Peter, T., Schlager,
1203 H., Cairo, F., Law, K. S., Shur, G. N., Belyaev, G. V., and Curtius, J.: In situ observations of new
1204 particle formation in the tropical upper troposphere: the role of clouds and the nucleation
1205 mechanism, *Atmos Chem Phys*, 11, 9983-10010, DOI 10.5194/acp-11-9983-2011, 2011.

1206 Weinheimer, A. J., Walega, J. G., Ridley, B. A., Sachse, G. W., Anderson, B. E., and Collins, J. E.:
1207 Stratospheric Noy Measurements on the Nasa Dc-8 during Aase-Ii, *Geophys Res Lett*, 20, 2563-
1208 2566, Doi 10.1029/93gl02627, 1993.

1209 Werner, A., Volk, C. M., Ivanova, E. V., Wetter, T., Schiller, C., Schlager, H., and Konopka, P.:
1210 Quantifying transport into the Arctic lowermost stratosphere, *Atmos Chem Phys*, 10, 11623-
1211 11639, DOI 10.5194/acp-10-11623-2010, 2010.

1212 Wilson, J. C., Stolzenburg, M. R., Clark, W. E., Loewenstein, M., Ferry, G. V., and Chan, K. R.:
1213 Measurements of Condensation Nuclei in the Airborne Arctic Stratospheric Expedition -
1214 Observations of Particle-Production in the Polar Vortex, *Geophys Res Lett*, 17, 361-364, Doi
1215 10.1029/Gl017i004p00361, 1990.

1216 Woiwode, W., Grooß, J.-U., Oelhaf, H., Molleker, S., Borrmann, S., Ebersoldt, A., Frey, W., Gulde, T.,
1217 Khaykin, S., Maucher, G., Piesch, C., and Orphal, J.: Denitrification by large NAT particles: the
1218 impact of reduced settling velocities and hints on particle characteristics, *Atmos. Chem. Phys.*
1219 *Discuss.*, 14, 5893-5927, 2014.

1220

1221

1222 **Figure captions**

1223 Figure 1: Model size distributions of stratospheric aerosol as provided in parameterized form by
1224 different sources: Jaenicke (1980), Wang et al. (1989) and Deshler (2008), and one size
1225 distribution published in Bardeen et al. (2008), from numerical simulations of meteoritic
1226 material ablated in the mesosphere and subsided to 30 km altitude. The grey shaded area
1227 denotes the range from maximum to minimum values of the size distributions that are used as
1228 the upper limit of the estimates described in Section 6. The size distribution resulting from
1229 numerical investigations serves as the lowermost limit of this estimate.

1230 Figure 2: Vertical distribution of particle mixing ratio N_{10} (left column), N_{10nv} (mid column) and
1231 resulting fraction f of non-volatile particles (right column) versus the potential temperature Θ
1232 for the EUPLEX campaign in 2003. Data are additionally subdivided (cf. Section 3) in period A
1233 (January-February, 2003) and period B (February – March, 2003). Data points for Θ above 400 K
1234 are color-coded according to ΔN_2O vortex index ξ_{vi} . For Θ below 400 K, data points are left in
1235 grey as inside or outside vortex apportioning is not unambiguous (cf. Section 2). Black lines
1236 indicate a regression over those data points which fulfill the inside-vortex criterion (Section 2).

1237 Figure 3: Structured as Figure 2 for the RECONCILE campaign in 2010 with a subdivision of the
1238 mission periods like for EUPLEX. Data are color-coded according to the ΔN_2O vortex index ξ_{vi} .
1239 For Θ below 400 K, data points are left in grey as the inside or outside vortex apportioning is not
1240 unambiguous (cf. Section 2). Black lines indicate a regression of data points that meet the inside-
1241 vortex criterion (Section 2).

1242 Figure 4: Structured as Figure 2 and Figure 3 for the ESSenCE campaign in 2011 with the color-
1243 coding of data according to the ΔN_2O vortex index ξ_{vi} . For Θ below 400 K, data points are left in
1244 grey as inside or outside vortex air cannot be apportioned unambiguously (cf. Section 2). Black
1245 lines indicate a regression of data points that fulfill the inside-vortex criterion (Section 2).

1246 Figure 5: Median vertical profiles of particle mixing ratios with 25- and 75-percentiles (bars) as
1247 function of potential temperature Θ . If whiskers are not visible the percentile range is covered
1248 by the size of data points. Data are attributed to either originate from inside (dots) or outside the
1249 vortex (circles) by using the ΔN_2O vortex index ξ_{vi} (cf. Section 2). Aerosol mixing ratios N_{10} , (left
1250 column), N_{10nv} (mid-left column), mixing ratio difference $N_{10} - N_{10nv}$ (mid-right column) and
1251 resulting fraction f of refractory particles (right column). Panels a) to d) from ESSenCe (i.e. the
1252 mission conducted the earliest in the winter season); Panels e) to h) data from EUPLEX; Panels i)
1253 to l) results from RECONCILE.

1254 Figure 6: Mixing ratio of non-volatile particles N_{10nv} and their fractional contribution f to
1255 measured total aerosol abundance as function of N_2O mixing ratio. The data points are colored
1256 according to the ΔN_2O vortex index ξ_{vi} . Data points are designated in grey if measurements
1257 occurred at Θ -levels below 400 K for which inside or outside vortex apportioning is not
1258 unambiguous (cf. Section 2). For data measured inside the vortex ($\xi_{vi} > 0.75$) the black lines
1259 indicate a linear correlation. Alternatively, for N_2O below 250 nmol mol⁻¹, curves representing a
1260 canonical correlation are provided as grey lines with the ESSenCe data (early winter) referring
1261 to conditions as closest to the pre-vortex situation (Panel a). The same early-winter climatology
1262 provides a reference for comparison to data from measurements in progressed winter (Panels b
1263 to e).

1264 Figure 7: Mixing ratio of non-volatile particles N_{10nv} as a function of potential temperature Θ
1265 (Panels a to c) and N_2O mixing ratio (Panels d to f) for measurements inside the vortex (i.e.
1266 where ΔN_2O vortex index $\xi_{vi} > 0.75$). Data points are color-coded by means of ΔN_2O vortex index
1267 in the range $0.75 < \xi_{vi} < 1$. Results are separated for Θ -levels below 410 K (crosses) and above
1268 410 K (dots) to account for the visible discontinuity (i.e. a transition zone) at the vortex bottom.
1269 Linear correlations are assumed for Θ -levels above 410 K and linear regressions are implied.
1270 These are separately displayed in Figure 8 for better comparability.

1271 Figure 8: Linear regressions with 95% confidence interval for the mixing ratio of non-volatile
1272 particles N_{10nv} as function of potential temperature Θ (Panel a) and N_2O mixing ratio (Panel b).
1273 Results from measurements within the vortex (ΔN_2O vortex index $\xi_{vi} > 0.75$) are shown for the
1274 three Arctic missions: EUPLEX (2003), RECONCILE (2010) and ESSenCe (2011).

1275

1276 **Figures**

1277

1278

1279

1280

1281

1282

1283

1284

1285

1286

1287

1288

1289

1290

1291

1292

1293

1294

1295

1296

1297

1298

1299

1300

1301

1302

1303

1304

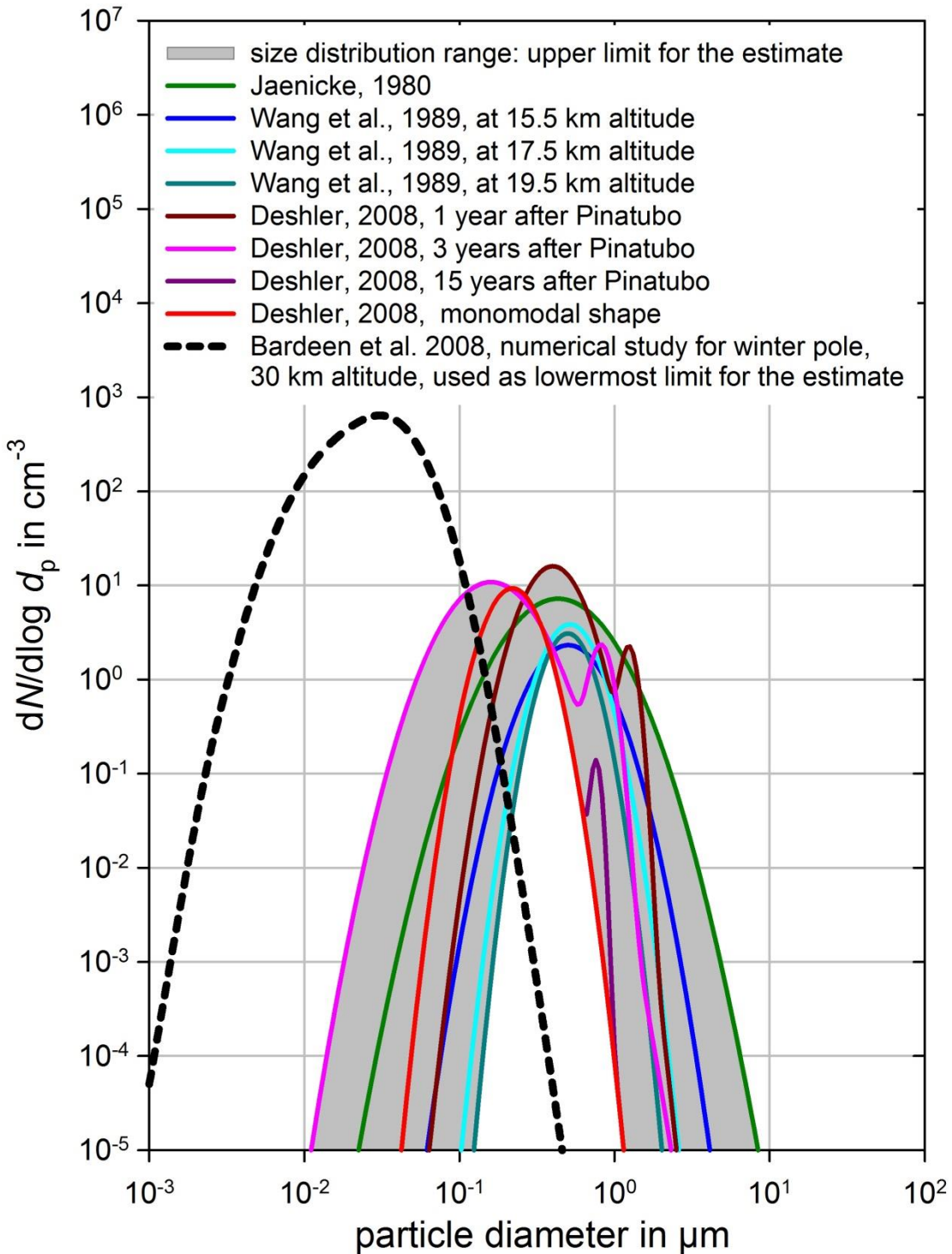


Figure 1

1305
 1306
 1307
 1308
 1309
 1310
 1311
 1312
 1313
 1314
 1315
 1316
 1317
 1318
 1319
 1320
 1321
 1322
 1323
 1324
 1325
 1326
 1327
 1328
 1329
 1330
 1331
 1332

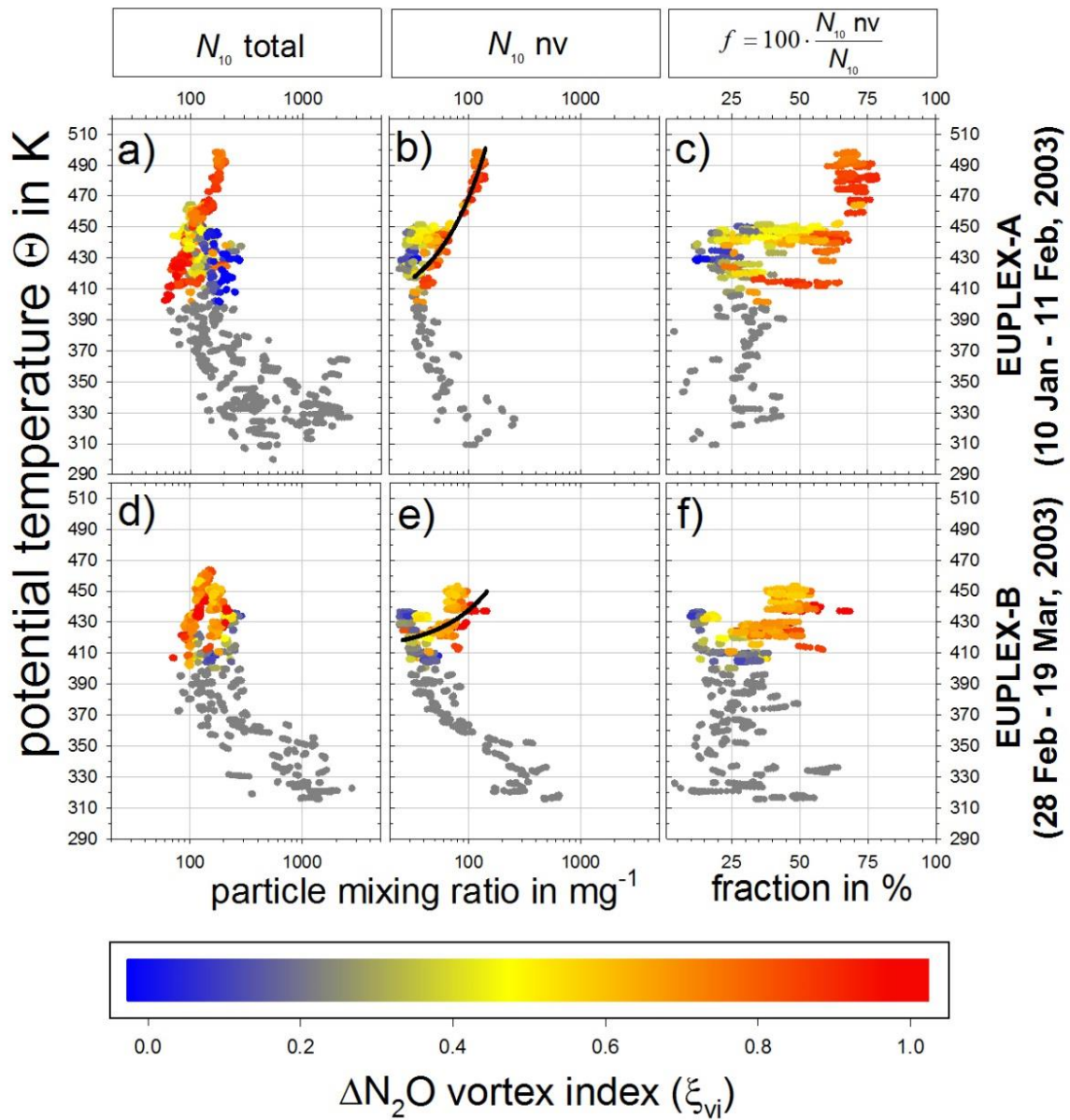


Figure 2

1333
 1334
 1335
 1336
 1337
 1338
 1339
 1340
 1341
 1342
 1343
 1344
 1345
 1346
 1347
 1348
 1349
 1350
 1351
 1352
 1353
 1354
 1355
 1356
 1357
 1358
 1359
 1360

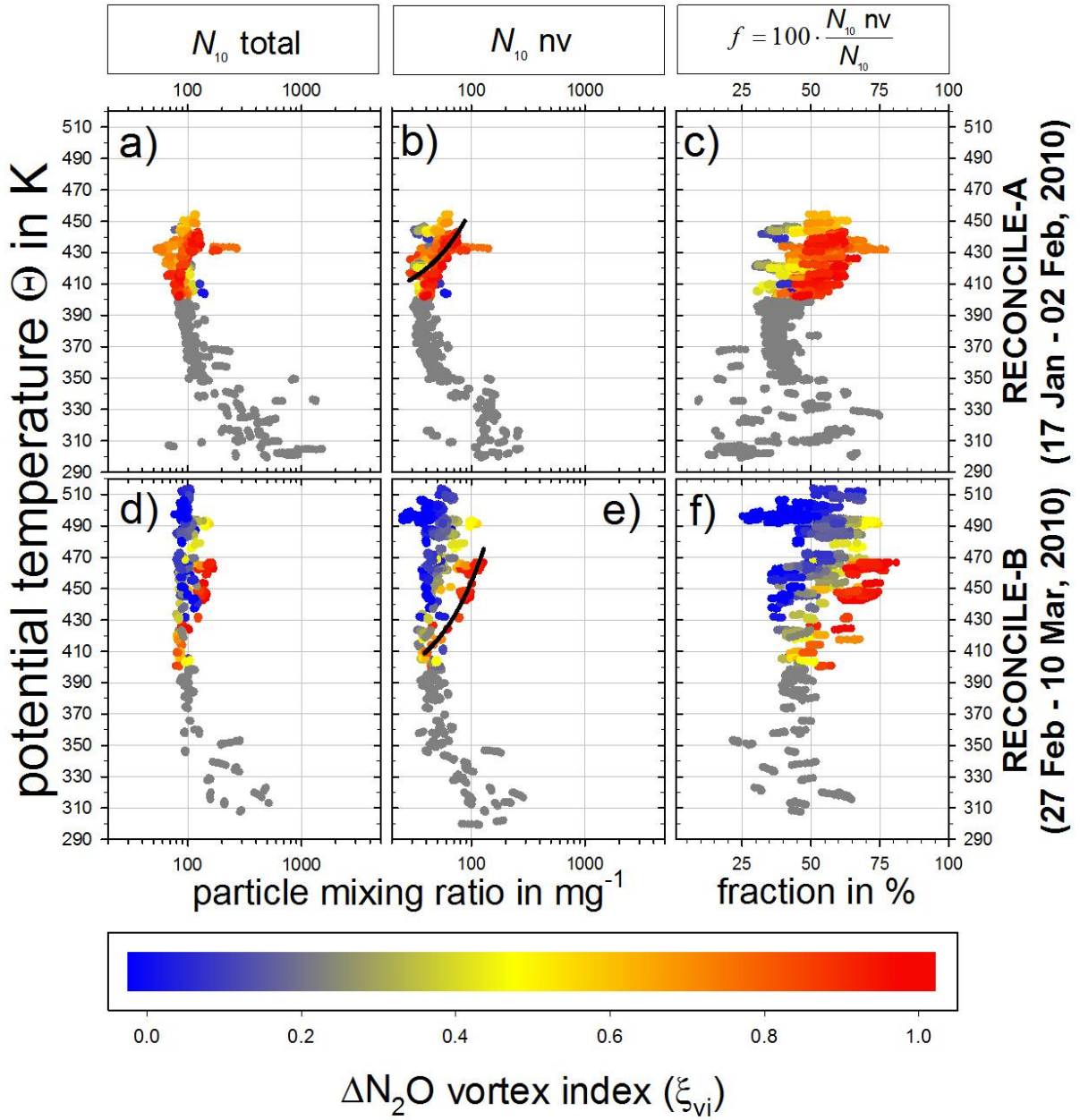


Figure 3

1361
1362
1363
1364
1365
1366
1367
1368
1369
1370
1371
1372
1373
1374
1375
1376
1377
1378
1379
1380
1381
1382
1383
1384
1385
1386
1387
1388

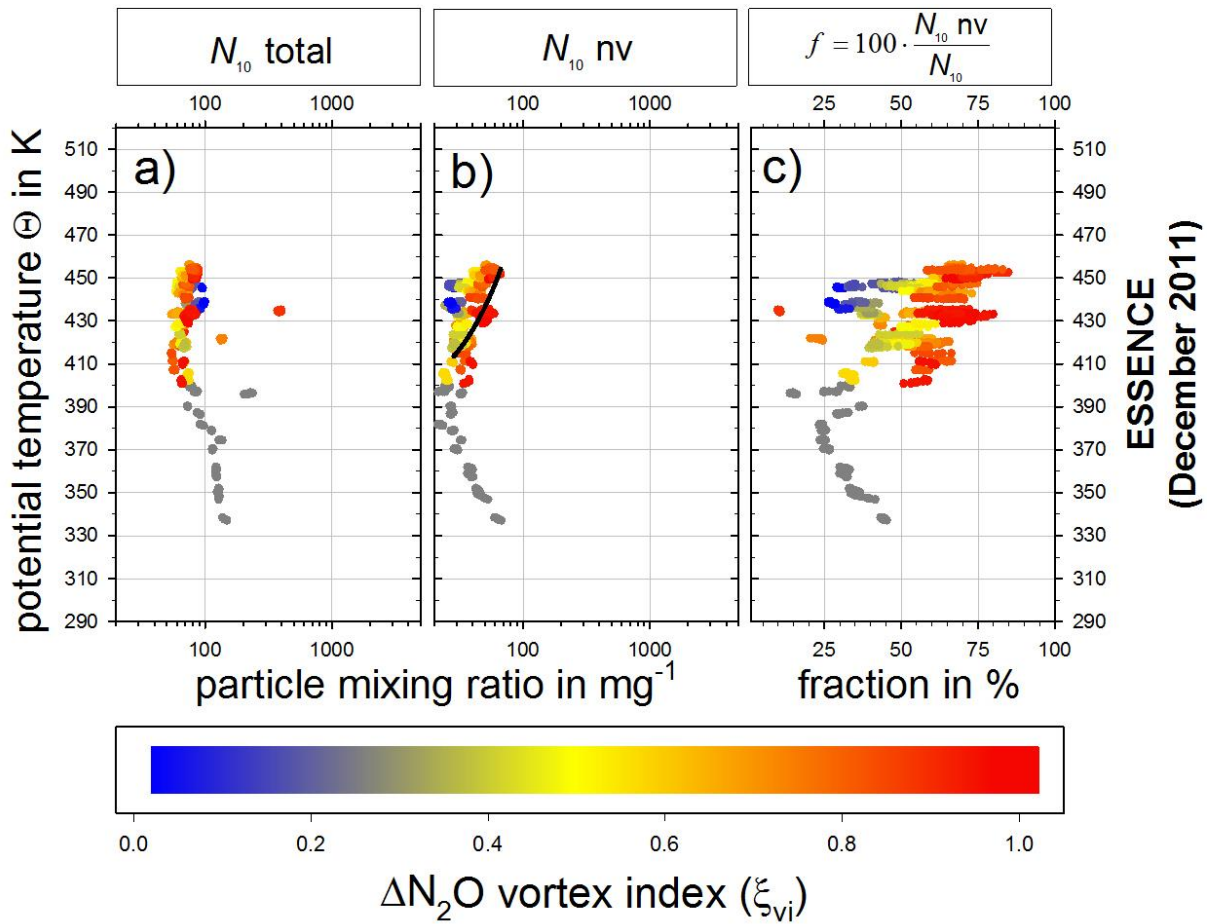


Figure 4

1389
 1390
 1391
 1392
 1393
 1394
 1395
 1396
 1397
 1398
 1399
 1400
 1401
 1402
 1403
 1404
 1405
 1406
 1407
 1408
 1409
 1410
 1411
 1412
 1413
 1414
 1415
 1416

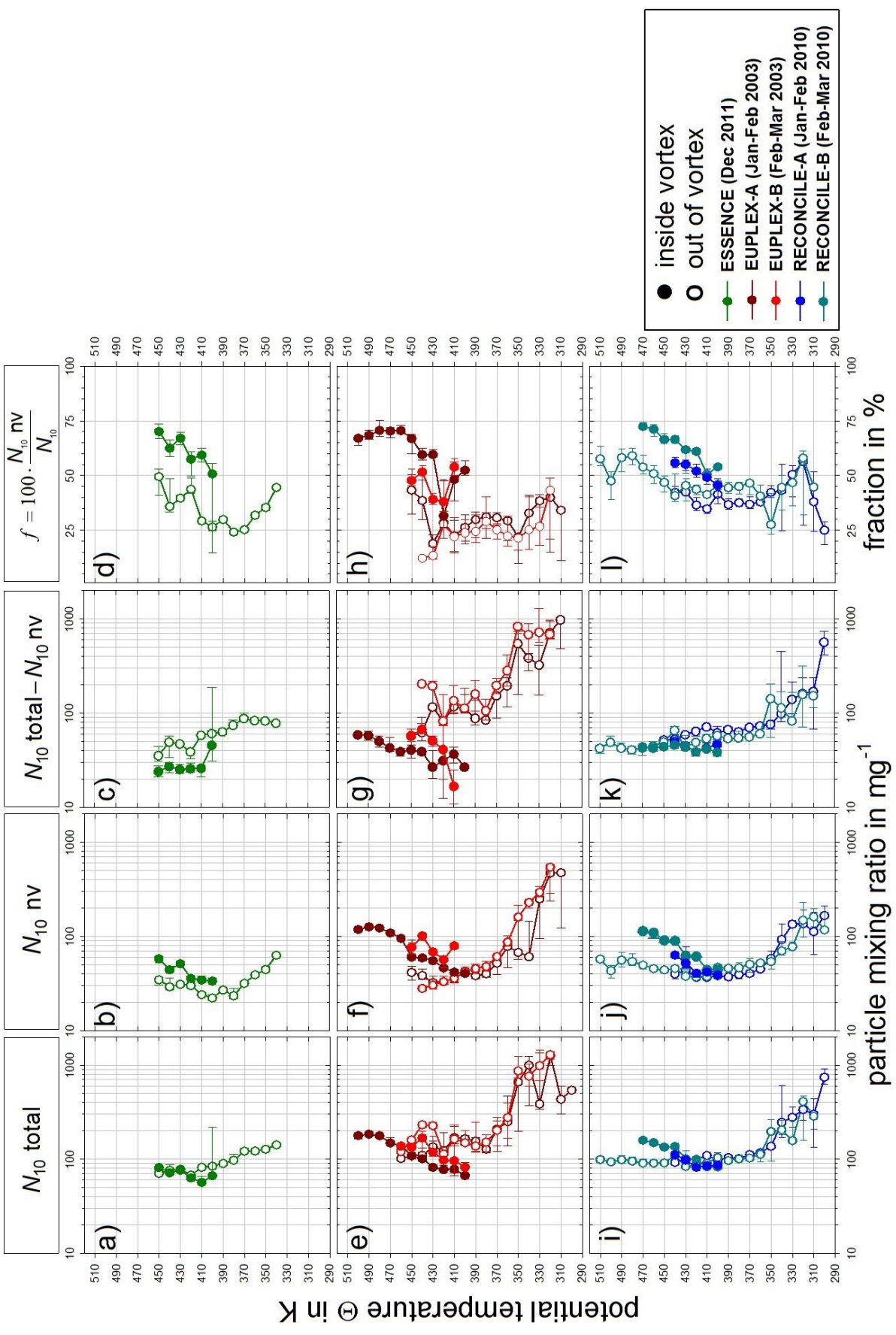


Figure 5

1417
 1418
 1419
 1420
 1421
 1422
 1423
 1424
 1425
 1426
 1427
 1428
 1429
 1430
 1431
 1432
 1433
 1434
 1435
 1436
 1437
 1438
 1439
 1440
 1441
 1442
 1443
 1444
 1445

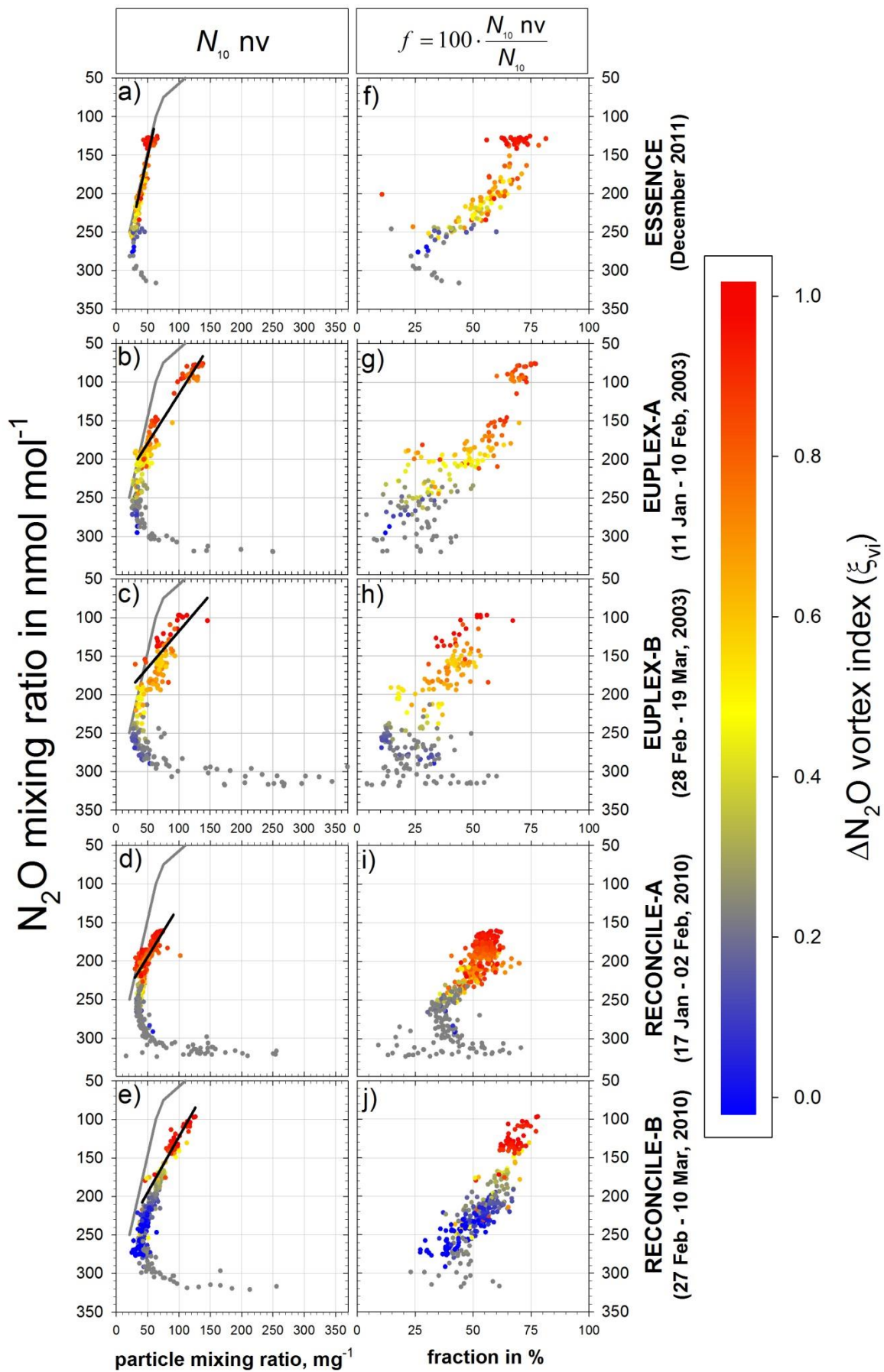


Figure 6

1446
1447
1448
1449
1450
1451
1452
1453
1454
1455
1456
1457
1458
1459
1460
1461
1462
1463
1464
1465
1466
1467
1468
1469
1470
1471
1472
1473

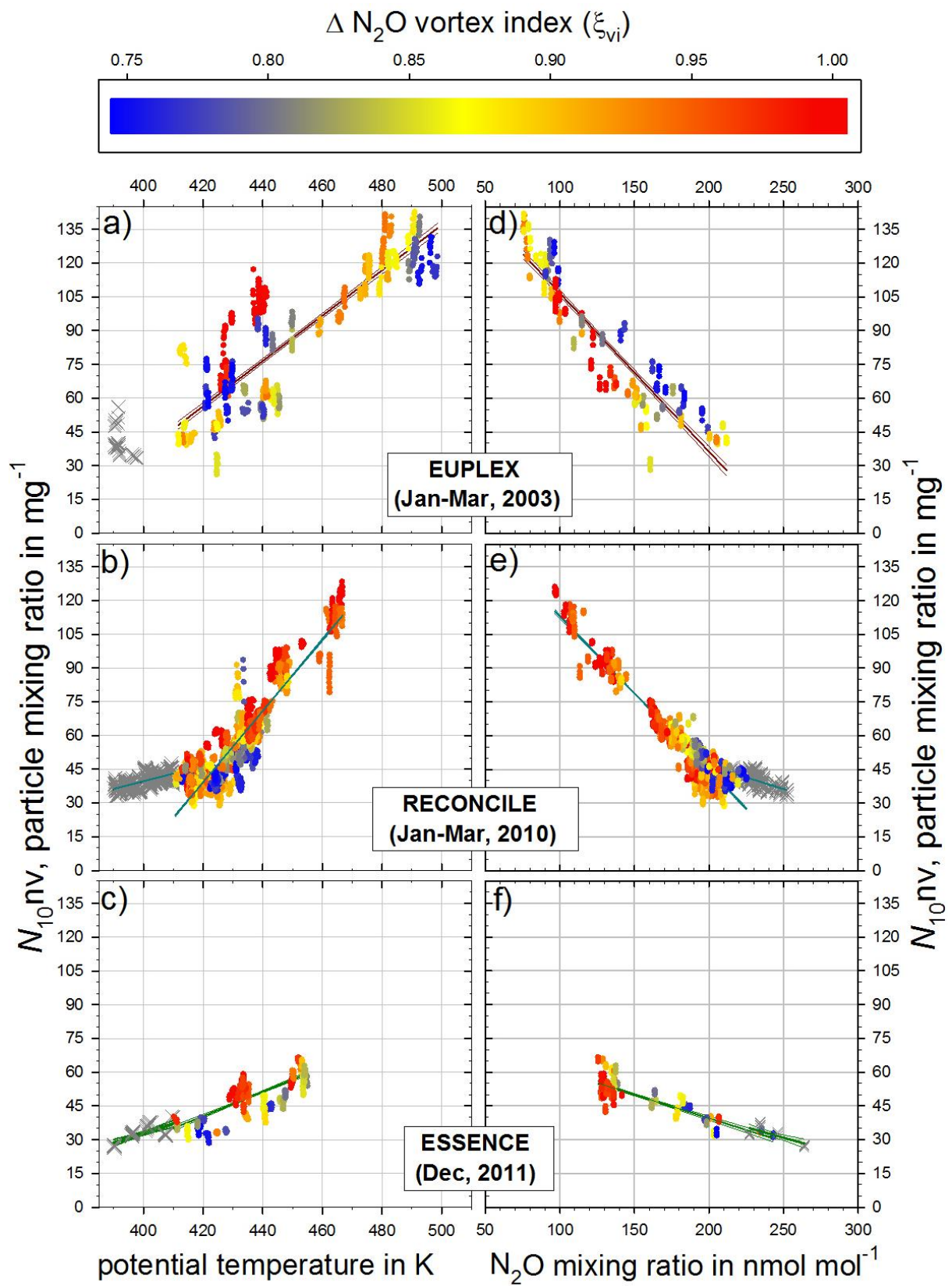


Figure 7

1474
1475
1476
1477
1478
1479
1480
1481
1482
1483
1484
1485
1486
1487
1488
1489
1490
1491
1492
1493
1494
1495
1496
1497
1498
1499
1500

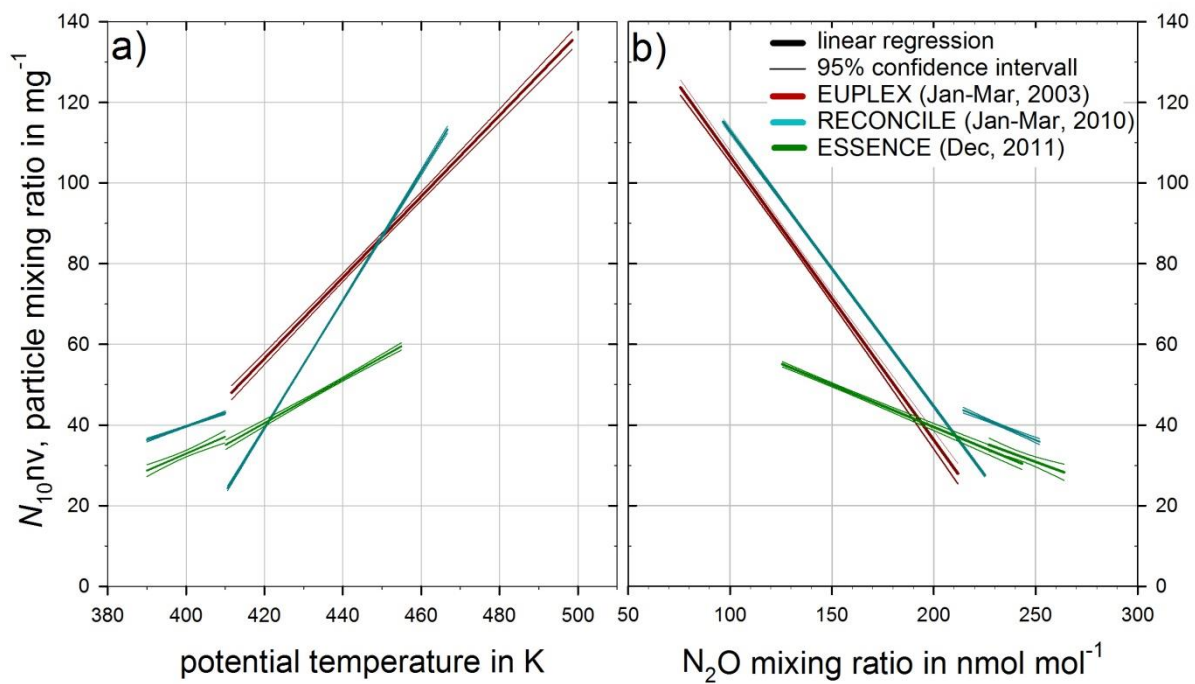


Figure 8

1501 **Tables**

1502

1503 **Table 1**

1504 Parameterization with standard error (σ) of the linear regression between the particle mixing
 1505 ratio N_{10nv} with potential temperature Θ and with N_2O mixing ratio for different altitude ranges,
 1506 $\Theta < 410$ K and $\Theta > 410$ K, respectively, within the vortex as displayed in Figure 8.

1507

1508 $y = f(x) = a x + b$ in mg^{-1} ;

1509 a_1, b_1 and correlation coefficient r^2_1 for $390 \text{ K} < \Theta \leq 410 \text{ K}$

1510 a_2, b_2 and correlation coefficient r^2_2 for $\Theta > 410 \text{ K}$

1511

	with $x = \Theta$ in K			with $x = N_2O$ in $nmol \text{ mol}^{-1}$		
	EUPLEX	RECONCILE	ESSenCe	EUPLEX	RECONCILE	ESSenCe
$a_1 \pm \sigma$	-	0.34 ± 0.02	0.42 ± 0.06	-	-0.21 ± 0.02	-0.19 ± 0.04
$b_1 \pm \sigma$	-	-96.3 ± 7.5	-135.6 ± 24.8	-	88.3 ± 3.9	77.3 ± 9.2
r^2_1	-	0.43	0.52	-	0.45	0.58
$a_2 \pm \sigma$	1.01 ± 0.02	1.56 ± 0.01	0.54 ± 0.02	-0.71 ± 0.05	-0.68 ± 0.01	-0.21 ± 0.01
$b_2 \pm \sigma$	-365.8 ± 8.9	-616.3 ± 5.3	-187.9 ± 9.3	178.5 ± 2.1	180.9 ± 1.1	81.4 ± 1.2
r^2_2	0.74	0.83	0.54	0.85	0.90	0.72

1512

1513

1514

1515

1516

1517 **Table 2**

1518 Estimated volume (v_p) of one refractory aerosol particle, particulate material density (ρ_p) and
 1519 parameterized $\Theta - p$ - relationship for the estimate of the total mass of refractory aerosol within
 1520 the air volume of the polar vortex (cf. Section 6).

1521

	v_p in m^3	ρ_p in $kg \text{ m}^{-3}$	p in hPa = $A + \exp(-C \cdot (\Theta \text{ in K} - B))$								
			EUPLEX			RECONCILE			ESSenCe		
			A	B	C	A	B	C	A	B	C
Mean	$5.00 \cdot 10^{-20}$	2000	46.1	550.5	0.0252	39.3	698.6	0.0149	46.0	557.6	0.0246
Min.	$8.71 \cdot 10^{-21}$	1000	31.8	594.7	0.0198	34.3	743.4	0.0125	38.8	592.3	0.0203
Max.	$1.86 \cdot 10^{-19}$	3000	30.8	753.8	0.0127	25.1	832.7	0.0110	4.87	823.0	0.0109

1522

1523

1524

1525

1526

1527

1528
1529
1530
1531
1532
1533
1534
1535
1536
1537

Table 3

Averaged vortex cross section areas from CLaMS analyses and resulting altitude-resolved refractory aerosol masses. The integrated aerosol masses inside the vortex are estimated from the in-situ measurements under the assumptions detailed in Section 6. This estimate provides an uppermost limit of refractory aerosol mass as it is based on size distributions of the background stratospheric aerosol parameterized from observations (cf. Section 2 and Jaenicke, 1980; Wang et al., 1989; Deshler, 2008). Vertical coordinates are given as potential temperatures and the corresponding pressure-ranges from the Θ - p -relationship are provided in Table 2. By applying specific uncertainty factors ($\sqrt{M_{nv}^{max}/M_{nv}^{min}}$) the extremes of involved uncertainties are covered. Indices (#) simplify the traceability of the data's origin in the text.

Θ in K	averaged vortex cross section area in km ²				altitude resolved mass of refractory aerosol based on size distribution of background stratospheric aerosol				
	EUPLEX		RECONCILE		EUPLEX		RECONCILE		ESSenCe
	p -range in hPa	M_{nv} in kg	p -range in hPa	M_{nv} in kg	p -range in hPa	M_{nv} in kg	p -range in hPa	M_{nv} in kg	
400	-	12873600	6437790	-	131 - 119	6.7×10 ⁶	101 - 89	2.5×10 ⁶	
410	10259900	15007800	7474930	85 - 77	119 - 108	2.2×10 ⁶	89 - 79	2.4×10 ⁶	
420	13184650	16898750	9309220	77 - 70	108 - 98	4.7×10 ⁶	79 - 72	2.7×10 ⁶	
430	15466600	18565200	11463200	70 - 64	98 - 90	7.0×10 ⁶	72 - 66	3.0×10 ⁶	
440	16893950	20123350	13472600	64 - 60	90 - 83	8.7×10 ⁶	66 - 62	3.1×10 ⁶	
450	18023400	21159700	14218900	60 - 57	83 - 77	9.9×10 ⁶	62 - 58	2.8×10 ⁶	
460	19140750	22579350	14915600	57 - 55	77 - 72	1.1×10 ⁷	58 - 56	2.5×10 ⁶	
470	20157300	23282300	-	55 - 53	72 - 67	1.1×10 ⁷	-	-	
480	21287700	-	-	53 - 51	-	-	-	-	
490	22248850	-	-	51 - 50	-	-	-	-	
500	23147150	-	-	50 - 49	-	-	-	-	
Summed mass of refractory aerosol in kg.									
total sum		(1)45.6×10 ⁶		(3)61.7×10 ⁶		(2)21.3×10 ⁶			
uncertainty factor		10.8		9.8		9.9			
sum (100-67 hPa)		15.5×10 ⁶		(4)48.1×10 ⁶		(5)10.6×10 ⁶			
uncertainty factor		9.8		(10)9.9		(11)9.2			

1538 **Table 4**
1539 Lowermost boundary for the estimates of the integrated refractory aerosol mass M in the vortex.
1540 Assumptions are the same as for previous calculation (cf. Section 6), as are the averaged vortex
1541 cross section areas from CLaMS as a function of Θ . This mass estimate is determined by a size
1542 distribution of meteoritic ablation material only over the winter pole resulting from numerical
1543 studies (Bardeen et al., 2008). Vertical coordinates are given as provided in Table 2. Uncertainty
1544 factors of ($\sqrt{M_{nv}^{max}/M_{nv}^{min}}$) are applied to cover the extremes of the involved uncertainties.
1545 Indices (#) simplify the traceability of the data's origin in the text.

altitude resolved mass of refractory aerosol based on
modelled size distribution of meteoritic ablation material (Bardeen et al., 2008)

Θ in K	EUPLEX		RECONCILE		ESSenCe	
	p -range in hPa	M_{nv} in kg	p -range in hPa	M_{nv} in kg	p -range in hPa	M_{nv} in kg
400	–	–	131 - 119	4.1×10^3	101 - 89	1.6×10^3
410	85 - 77	2.7×10^3	119 - 108	1.4×10^3	89 - 79	1.5×10^3
420	77 - 70	3.3×10^3	108 - 98	2.9×10^3	79 - 72	1.7×10^3
430	70 - 64	3.5×10^3	98 - 90	4.3×10^3	72 - 66	1.8×10^3
440	64 - 60	3.5×10^3	90 - 83	5.4×10^3	66 - 62	1.9×10^3
450	60 - 57	3.2×10^3	83 - 77	6.2×10^3	62 - 58	1.7×10^3
460	57 - 55	3.0×10^3	77 - 72	6.8×10^3	58 - 56	1.6×10^3
470	55 - 53	2.7×10^3	72 - 67	7.1×10^3	–	–
480	53 - 51	2.4×10^3	–	–	–	–
490	51 - 50	2.1×10^3	–	–	–	–
500	50 - 49	1.8×10^3	–	–	–	–
total sum		28.3×10^3		41.5×10^3		14.7×10^3
uncertainty factor		2.3		2.1		2.1
sum (100-67 hPa)		9.6×10^3		⁽⁶⁾ 29.8×10^3		⁽⁷⁾ 6.5×10^3
uncertainty factor		2.1		2.1		1.9

1546